

# Particle-Size-Grouping Model of Precipitation Kinetics in Microalloyed Steels

KUN XU and BRIAN G. THOMAS

The formation, growth, and size distribution of precipitates greatly affects the microstructure and properties of microalloyed steels. Computational particle-size-grouping (PSG) kinetic models based on population balances are developed to simulate precipitate particle growth resulting from collision and diffusion mechanisms. First, the generalized PSG method for collision is explained clearly and verified. Then, a new PSG method is proposed to model diffusion-controlled precipitate nucleation, growth, and coarsening with complete mass conservation and no fitting parameters. Compared with the original population-balance models, this PSG method saves significant computation and preserves enough accuracy to model a realistic range of particle sizes. Finally, the new PSG method is combined with an equilibrium phase fraction model for plain carbon steels and is applied to simulate the precipitated fraction of aluminum nitride and the size distribution of niobium carbide during isothermal aging processes. Good matches are found with experimental measurements, suggesting that the new PSG method offers a promising framework for the future development of realistic models of precipitation.

DOI: 10.1007/s11661-011-0938-y

© The Minerals, Metals & Materials Society and ASM International 2011

## I. INTRODUCTION

THE demand for steels with higher strength, ductility, and toughness is always increasing. Many alloying additions act to improve these properties through the formation of precipitate particles. In addition to precipitation strengthening, precipitates often act by pinning grain boundaries and inhibiting grain growth. These effects depend on both the volume fraction and size distribution of the precipitates.<sup>[1–4]</sup> Many small particles are more effective than a few large particles. An unfortunate side effect is a decrease in high-temperature ductility and possible crack formation during processes such as casting and hot rolling, caused by the growth of voids around precipitate particles on the weak grain boundaries. It is, therefore, important to control the spatial distribution, morphological characteristics, and size distribution of precipitates during all stages of steel processing. These parameters are generally determined by the alloy composition, and temperature history. In high-deformation processes such as rolling, they also depend strongly on strain and strain rate.

The accurate modeling of precipitate growth includes at least two analysis steps: (1) supersaturation, based on equilibrium precipitation thermodynamics and (2) kinetic effects. Many models to predict equilibrium precipitation are available in commercial packages based on minimizing Gibbs free energy, including Thermo-Calc (Thermo-Calc Software, Stockholm, Sweden),<sup>[5,6]</sup> FactSage (Center for Research in Computational

Thermochemistry, Montreal, Canada),<sup>[7]</sup> ChemSage (GTT-Technologies, Aachen, Germany),<sup>[8]</sup> JMatPro (Sente Software, Guildford, United Kingdom),<sup>[9]</sup> other CALPHAD models,<sup>[10,11]</sup> and other thermodynamic models based on solubility products in previous literature.<sup>[12–16]</sup> A recent equilibrium model predicts the stable formation of typical oxides, sulfides, nitrides and carbides in microalloyed steels efficiently by solving the fully coupled nonlinear system of solubility-product equations.<sup>[17]</sup> The model has been validated with analytical solutions of simple cases, results of a commercial package, and previous experimental results. A useful equilibrium model must predict accurately the occurrence and stability of precipitates, their equilibrium amounts, and compositions for different steel compositions, phases, and temperatures to calculate the supersaturation/driving force for a kinetic model.

Theoretically, precipitates start to form when the solubility limit is exceeded, but reaching equilibrium usually takes a long time. For most steel processes, especially at lower temperatures, equilibrium is seldom approached due to limited time. Thus, kinetic models of precipitate growth are a practical necessity for realistic predictions.

An early effort to predict phase transformation kinetics is the KJMA model, by Kolmogorov,<sup>[18]</sup> Johnson and Mehl,<sup>[19]</sup> and Avrami,<sup>[20]</sup> which is used widely to study precipitation processes and to generate time-temperature-transformation diagrams. The general isothermal KJMA equation to describe transformed fraction  $f$  as a function of time  $t$  is given by<sup>[21]</sup>

$$f(t) = 1 - \exp(-K \cdot t^n) \quad [1]$$

where  $K$  is the rate function for nucleation and growth that depends on chemical composition and temperature and  $n$  is the Avrami exponent, typically ranging from

---

KUN XU, Graduate Student, and BRIAN G. THOMAS, C.J. Gauthier Professor, are with the Mechanical Science and Engineering Department, University of Illinois at Urbana-Champaign, Urbana, IL 61801. Contact e-mail: bgthomas@illinois.edu

Manuscript submitted October 10, 2010.

Article published online October 19, 2011

1 to 4, which depends on growth dimensionality (one dimensional, two dimensional, and three dimensional), nucleation index (zero, decreasing, constant, or increasing nucleation rate), and growth index (interface-controlled or diffusion-controlled). The parameters  $K$  and  $n$  are determined from experimental measurements at different test temperatures and compositions, and often they vary during precipitation. Although this model can match many precipitated fraction measurements,<sup>[22,23]</sup> its empirical nature prevents it from describing alternate thermomechanical processes without refitting the parameters with further measurements. Moreover, size distributions are not predicted with this model.

Precipitates can form at many different stages and locations during metal refining, casting, and thermal processing, including in the liquid metal because of collision, the mushy-zone between dendrites because of rapid diffusion during solidification, and on the grain boundaries or inside the grains because of slow solid-state diffusion. This process results in different compositions, shapes, and size distributions of precipitates, which greatly influence product quality. Precipitate particles grow via two major mechanisms: (1) collision in the liquid and (2) diffusion in both liquid and solid. Both mechanisms have been studied extensively, and better computational models are now available with fast improved computer power in recent decades.

Collisions between particles and rapid diffusion in the liquid phase increase the number of large particles and enhance inclusion removal by flotation. The evolution of particle concentration and size distribution because of collisions has been modeled using the collision frequency between particles per unit volume of liquid medium,<sup>[24]</sup> and such models have been applied successfully for various collision mechanisms, including turbulent collision,<sup>[25]</sup> Stokes collision,<sup>[26]</sup> Brownian collision,<sup>[27]</sup> and gradient collision.<sup>[28]</sup>

The entire diffusion-controlled precipitation process in the solid is separated classically into three stages: nucleation, growth, and coarsening. The nucleation stage includes an induction period to form stable nuclei. It is based on the critical embryo size needed for the volume-energy decrease to exceed the surface-energy increase and a time-dependent Arrhenius relation to describe the nucleation rate.<sup>[29]</sup> Such a classic model of steady-state nucleation has been applied successfully to predict the start times of strain-induced Ti(C,N) precipitation in austenite,<sup>[30]</sup> as measured via stress relaxation experiments.<sup>[31]</sup>

After nucleation, particles of all sizes can grow because of the high supersaturation that defines the growth stage. After the nucleation and growth stages, precipitates of various sizes are dispersed in the matrix phase. Once the supersaturation has decreased to equilibrium, the solute concentrations in the matrix and at the particle/matrix interface are comparable and capillary effects become dominant, causing coarsening or Ostwald ripening.<sup>[32]</sup> Governed by the minimization of the total surface energy, coarsening is driven by the difference in concentration gradients near precipitate particles of different sizes. The larger particles are surrounded by low concentration; they grow by

diffusion from the high concentration surrounding smaller particles, which are less stable and shrink. Thus, the net number density of all particles now decreases with time.

Each of these three stages is dominated by different mechanisms, and particle size evolution follows different laws. Coarsening increases with time according to the mean particle size cubed,<sup>[33,34]</sup> according to LSW theory, which is slower than the square relation during the growth stage.<sup>[35]</sup> More discussion is given elsewhere on classic nucleation,<sup>[36]</sup> growth,<sup>[37]</sup> and coarsening<sup>[38]</sup> phenomena.

Growth and coarsening are often treated as one continuous and competing process, assuming a Gibbs-Thomson exponential relation for interface concentration with particle size.<sup>[39]</sup> Together with a classic nucleation model, these models describe the volume fraction and size distribution of precipitates evolving with time.<sup>[40]</sup> Such combinations of classic models have been applied to simulate the precipitation of AlN in matrix and grain boundary of low-carbon steels,<sup>[41]</sup> and NbC on dislocation in ferrite.<sup>[42]</sup>

Taking advantage of faster computers, more computational models of precipitation kinetics have been developed recently. The most fundamental method is solving the quantum mechanics equations.<sup>[43,44]</sup> At the atomic scale, kinetic Monte Carlo models describe diffusion statistically through vacancy jumps and have been applied to calculate precipitation, such as Al<sub>3</sub>Zr and Al<sub>3</sub>Sc in aluminum<sup>[45]</sup> and Y<sub>2</sub>O<sub>3</sub> in ferrite.<sup>[46]</sup> However, these small-scale models are only suitable for fine particles, such as at the nucleation stage. Phase field methods are based on minimization of free energy and have been applied to calculate the interface dynamics and effects such as strain, interface curvature, and diffusivity on growth of an isolated precipitate in a supersaturated matrix,<sup>[47,48]</sup> such as M<sub>23</sub>C<sub>6</sub> carbide in steel.<sup>[49]</sup> Recently, a commercial precipitation-kinetics software package, Matcalc, was developed based on thermodynamic extremum principles, and it was applied to simulate multiphase precipitation kinetics in multicomponent systems, including separate models within the matrix<sup>[50,51]</sup> and on grain boundaries.<sup>[52]</sup> Cluster dynamics model precipitation using mesoscopic clusters, also called “nanoparticles,” so these models potentially can link between atomistic simulations and macroscopic models. This method does not require explicit laws for the nucleation, growth and coarsening stages, and considers the condensation and evaporation rates between neighboring clusters, based on a thermodynamic model of the free energy of the system.<sup>[53–55]</sup>

Molecule-based models such as Smoluchowski<sup>[24]</sup> for collision and Kampmann and Kahlweit<sup>[56]</sup> for diffusion are attractive because (1) the particles evolve automatically without any explicit laws for the different stages, (2) particles of all sizes are tracked, and (3) the few parameters are fundamental physical constants themselves. Unfortunately, these models encounter inevitable difficulties when they are applied to simulate practical processes, where the precipitate particle size ranges greatly from a single “pseudomolecule” of ~0.1 nm to coarsened particles larger than 100 μm. A pseudomolecule (or called a “monomer” in collision models<sup>[57,58]</sup>) is

a stoichiometric cluster of atoms that consists of as few as a single metallic/interstitial atom pair. Random thermal diffusion creates unstable clusters of chemically bonded pseudomolecules called “embryos,” which grow into stable “nuclei” if they exceed a critical size. Realistic particles range in size over at least 6 orders of magnitude and contain from 1 to  $10^{18}$  pseudomolecules. With such an overwhelming linear scale, it is impossible to solve realistic problems using traditional models based on molecules.

Attempting to overcome this difficulty, the particle-size-grouping (PSG) method has been introduced in several previous studies and has proven to be effective in calculating the evolution of particle size distributions for collision-coagulation growth over a large size range.<sup>[59–64]</sup> Rather than track each individual particle size, the main idea of this technique is to divide the entire possible particle size range into a set of size “groups,” each with a specific mean size and size range. Careful attention is required to formulate the equations to ensure proper interaction and mass conservation.<sup>[59]</sup> Several researchers applied this PSG method to simulate inclusion agglomeration in liquid steel caused by collisions, coagulation, and removal. Such models have been applied to RH degassers,<sup>[60]</sup> continuous casting tundishes,<sup>[61,62]</sup> and ladle refining.<sup>[63,64]</sup> To start these PSG models, an initial size distribution is still required, which can be found from either experimental measurements or assumptions.

To make the PSG method more usable, Nakaoka *et al.*<sup>[65]</sup> used different volume ratios between neighboring size groups, taking advantage of the exponential increase in sizes that accompany powers of 2. This innovation allows modeling from single pseudomolecules to realistic particle sizes with only 20 to 80 size groups. Particle collisions were modeled considering both intergroup and intragroup interactions, and numerical results agreed well with experimental agglomeration curves. However, little work has been done to apply the PSG method to diffusion, which is the dominant mechanism for precipitate growth in many processes including steel casting and rolling. One study by Zhang and Pluschkell<sup>[66]</sup> coupled both collision and diffusion into a PSG model, but inter-group diffusion was not considered. Zhang and colleagues<sup>[57,58]</sup> included a discrete-sectional technique by Gelbard *et al.*<sup>[67]</sup> and Wu and Flagan<sup>[68]</sup> into the PSG model, but this weakens the efficiency of the method and the accuracy of the treatment of diffusion. The insurance of mass conservation has not been verified. No previous study has demonstrated accurate simulation of diffusion using a PSG method.

The purpose of the current study is to develop accurate, robust, and versatile PSG methods to simulate precipitate growth from both collision and diffusion mechanisms. The standard PSG method for collision problem is developed first, and then a new PSG method for diffusion is created. Both methods are verified by comparison with exact solutions of the primary population equations in test problems. The new PSG method is shown to be a time-efficient calculation with complete mass balance and high accuracy. Finally, the new PSG

method is applied to simulate several practical precipitation processes in solid steels and is compared with experimental measurements.

## II. PARTICLE COLLISION MODEL

The population balance model for collision first suggested by Smoluchowski<sup>[24]</sup> is

$$\frac{dn_i}{dt} = \frac{1}{2} \sum_{k=1}^{i-1} \Phi_{k,i-k} n_k n_{i-k} - n_i \sum_{k=1}^{\infty} \Phi_{i,k} n_k \quad [2]$$

where  $n_i$  is the number of size  $i$  particles per unit volume or “number density” and  $\Phi_{i,j}$  is the collision frequency between size  $i$  and size  $j$  particles. The first term on the right-hand side generates size  $i$  particles because of the collision of two smaller particles, and the second term decreases the number of size  $i$  particles by their collision with particles of any size to become larger particles. The generation term is halved to avoid counting collision pairs twice. However, when two particles generating size  $i$  particles have same size, the generation term should not be halved because the collision pair is unique. Moreover, the loss term should be doubly counted when size  $i$  particles collide with themselves. The number of pseudomolecules composing the largest agglomerated particle must be a finite number  $i_M$  in numerical computation. Making these appropriate changes gives the following improved expression:

$$\frac{dn_i}{dt} = \frac{1}{2} \sum_{k=1}^{i-1} (1 + \delta_{k,i-k}) \Phi_{k,i-k} n_k n_{i-k} - n_i \sum_{k=1}^{i_M} (1 + \delta_{i,k}) \Phi_{i,k} n_k \quad [3]$$

where  $\delta_{i,k}$  is the Kronecker delta,  $\delta_{i,k} = 1$  for  $i = k$ , and  $\delta_{i,k} = 0$  for  $i \neq k$ . When  $i = 1$ , the population balance for dissolved single pseudomolecules simplifies to

$$\frac{dn_1}{dt} = -n_1 \sum_{k=1}^{i_M} (1 + \delta_{1,k}) \Phi_{1,k} n_k \quad [4]$$

Thus, the number density of single pseudomolecules always decreases with collisions. Evaluating Eqs. [3] and [4] requires summing over and tracking every possible size from 1 to  $i_M$  pseudomolecules, so it is not practical for realistic particle sizes. The results from these equations, however, comprise the exact solution for collision test problems.

## III. PRECIPITATE PARTICLE DIFFUSION MODEL

Kampmann and Kahlweit<sup>[56]</sup> suggested the following diffusion-controlled model to treat the kinetics of nucleation, growth, and coarsening as one continuous and simultaneous process:

$$\frac{dn_i}{dt} = -\beta_i n_1 n_i + \beta_{i-1} n_1 n_{i-1} - \alpha_i A_i n_i + \alpha_{i+1} A_{i+1} n_{i+1} \quad (i \geq 2) \quad [5]$$

where  $\beta_i$ ,  $\alpha_i$ , and  $A_i$  are the diffusion growth rate, dissociation rate, and reaction sphere surface area for a size  $i$  particle containing  $i$  pseudomolecules. The first and second terms on the right-hand side account for the loss and generation of size  $i$  particles from “diffusion growth” by adding a single pseudomolecule to size  $i$  and  $i - 1$  particles, respectively. The third and fourth terms account for the loss and generation of size  $i$  particles from particle “dissociation” by losing a single pseudomolecule from size  $i$  and  $i + 1$  particles, respectively. For single pseudomolecules,  $i = 1$ , the special cases of double loss when two pseudomolecules react with each other and double generation of single pseudomolecules when size 2 particles dissociate are not counted exactly in Kampmann’s initial work. Thus, the following revised balance equation is suggested:

$$\frac{dn_1}{dt} = -n_1 \sum_{k=1}^{i_M} (1 + \delta_{1,k}) \beta_k n_k + \sum_{k=2}^{i_M} (1 + \delta_{2,k}) \alpha_k A_k n_k \quad [6]$$

Assuming a uniform spherical concentration field of single pseudomolecules with a boundary layer thickness approximated by  $r_i$  around each size  $i$  particle, the diffusion growth rate of size  $i$  particles is expressed by<sup>[56]</sup>

$$\beta_i = 4\pi D r_i \quad [7]$$

where  $D$  is the diffusion coefficient in the matrix phase and  $r_i$  is the radius of size  $i$  particles. As precipitation reactions always involve more than one element, this coefficient is chosen for the slowest-diffusing element, which is assumed to control the diffusion rate. Because the diffusion of interstitial elements such as O, S, N, and C is much faster, usually the diffusion rate is determined by the diffusion coefficient of the alloying metal element in the precipitate.

The following relation is assumed for the dissociation rate, which is the number of pseudomolecules lost per unit surface area of size  $i$  particles per unit time, based on a mass balance of a particle in equilibrium with the surrounding matrix phase<sup>[56]</sup>:

$$\alpha_i = \beta_i n_{1i} / A_i = D n_{1i} / r_i \quad [8]$$

The concentration of single pseudomolecules  $n_{1i}$  in equilibrium around the surface of the size  $i$  particle is needed to evaluate this equation. This is estimated using the Gibbs-Thomson equation and decreases with increasing particle size as follows<sup>[39]</sup>:

$$n_{1i} = n_{1,\text{eq}} \exp\left(\frac{2\sigma V_P}{R_g T r_i}\right) \quad [9]$$

where  $n_{1,\text{eq}}$  is the number density of dissolved single pseudomolecules in equilibrium with a plane interface of the precipitate phase,  $\sigma$  is the interfacial energy between the precipitate particles and the matrix phase,  $V_P$  is the molar volume of the precipitate,  $R_g$  is the gas constant, and  $T$  is the absolute temperature. This equation

indicates that increasing particle radius causes the nearby solute concentration to decrease greatly, by several orders of magnitude.

Equations [5] through [9] include the effects of equilibrium, diffusion growth, dissociation, curvature effects, and mass conservation, with parameters all having appropriate physical significance. The results from these equations are regarded as the exact solution for diffusion test problems.

#### IV. PARTICLE-SIZE-GROUPING (PSG) METHOD

From a theoretical point of view, these molecule-based population-balance models in the previous sections are accurate, and the integration of their set of governing equations is straightforward. However, the computational cost quickly becomes infeasible for realistic particle sizes. The PSG method is introduced here to overcome this difficulty. The fundamental concept of the PSG method is shown schematically in Figure 1. In this method, the particles are divided into different size groups (size group number  $j$ ) with characteristic volume  $V_j$  and characteristic radius  $r_j$ . The number density of particles of size group  $j$  is defined as

$$N_j = \sum_{V_{j+1} > V > V_{j-1}} n(V) \quad [10]$$

This summation covers all particles whose volume lies between two threshold values. The threshold volume that separates two neighboring size groups,  $V_{j,j+1}$ , is assumed to be the geometric average of the characteristic volumes of these two groups, instead of the arithmetic average used in previous works<sup>[65,66]</sup>

$$V_{j,j+1} = \sqrt{V_j V_{j+1}} \quad [11]$$

If a newly generated particle has its volume between  $V_{j-1,j}$  and  $V_{j,j+1}$ , it is counted in size group  $j$ . The increase of number density of size group  $j$  particles is then adjusted according to the difference between the volume of the new particle and  $V_j$  to conserve mass.

The volume ratio between two neighboring size groups is defined as

$$R_V = \frac{V_{j+1}}{V_j} \quad [12]$$

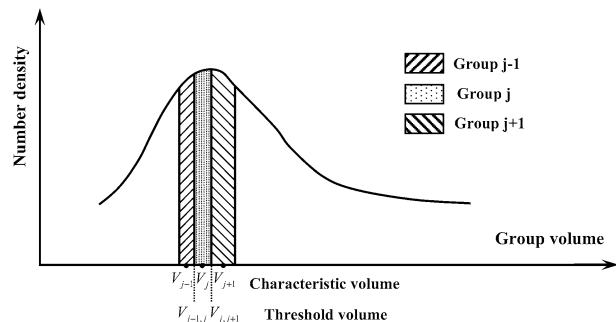


Fig. 1—The schematic of particle size distribution in PSG method.

To generate regularly spaced threshold values,  $R_V$  is usually varied. However, for constant  $R_V$ , the PSG characteristic and threshold volumes can be expressed as

$$V_j = R_V^{j-1} V_1, V_{j,j+1} = R_V^{(j-1/2)} V_1 \quad [13]$$

where the volume of a single pseudomolecule  $V_1$  is computed using the molar volume of its precipitate crystal structure  $V_P$

$$V_1 = \frac{V_P}{N_A} \quad [14]$$

where  $N_A$  is Avogadro's number and the small effects of temperature change and vacancies are neglected. Because the particle volume is calculated from a bulk property  $V_P$ , consideration of the packing factor is not needed. The number of pseudomolecules contained in a given PSG volume is

$$\frac{dN_j}{dt} = \underbrace{N_j \sum_{k=1}^{k_{c,j}} \frac{V_k}{V_j} \Phi_{j,k} N_k}_{\text{Group } j \text{ colliding with smaller particles}} - \underbrace{N_j \sum_{k=k_{c,j}+1}^{G_M} [(1 + \delta_{j,k}) \Phi_{j,k} N_k]}_{\text{Group } j \text{ colliding with larger particles}} + \underbrace{\sum_{k=k_{c,j}}^{j-1} \frac{V_{j-1} + V_k}{V_j} \Phi_{j-1,k} N_{j-1} N_k}_{\text{Group } j-1 \text{ colliding with particles from group } j-1} \quad (j \geq 2) \quad [18]$$

$$m_j = \frac{V_j}{V_1}, m_{j,j+1} = \frac{V_{j,j+1}}{V_1} \quad [15]$$

In the PSG method, it is easy to introduce fractal theory to consider the effect of particle morphology. The effective radius of a particle can be expressed by

$$r_j = r_1 \left( \frac{V_j}{V_1} \right)^{1/D_f} \quad [16]$$

where  $D_f$  is the fractal dimension, which can vary from 1 (needle-shaped precipitates) to 3 (complete coalescence into smooth spheres). Tozawa *et al.*<sup>[69]</sup> proposed  $D_f = 1.8$  for  $\text{Al}_2\text{O}_3$  clusters in liquid steel, and  $D_f = 3$  is adopted everywhere in this work for simplicity.

After the number of single pseudomolecules composing the largest agglomerated particles  $i_M$  is determined, the corresponding total number of size groups  $G_M$  must be large enough for the second largest size group to contain the largest agglomerated particle  $i_M$ . Thus, for constant  $R_V$ ,  $G_M$  must satisfy

$$G_M \geq \text{ceil}(\log_{R_V} i_M) + 2 \quad [17]$$

The largest size group is a boundary group that always has zero number density. The accuracy of the PSG method should increase with decreasing  $R_V$ , as more size groups are used. From the logarithm relation

shown in Eq. [17], it can be observed that the PSG method is efficient for real problems with a large range of particle sizes.

### A. PSG Method for Collision

Applying the PSG method to model colliding particles involves the following rules, affecting size group  $j$ :

- A size group  $j$  particle colliding with a small particle, from group 1 to  $k_{c,j}$ , remains in group  $j$  and increases the number density  $N_j$ .
- A group  $j$  particle colliding with a relatively large particle, from a group larger than  $k_{c,j}$ , generates a particle in group  $j + 1$  or higher.
- A group  $j - 1$  particle colliding with a particle from group  $k_{c,j}$  to  $j - 1$  generates a group  $j$  particle.

Combining these rules gives the following equation, where the coefficients involving mean volumes are needed to conserve volume

$$\text{with } k_{c,j} = \begin{cases} j-1 & 4.000 > R_V > 2.148 \\ j-2 & 2.148 > R_V > 1.755 \\ j-3 & 1.755 > R_V > 1.587 \end{cases} \quad [19]$$

The  $R_V$  ranges in Eq. [19] are found by solving the following equations, after inserting the Eq. [13] expressions:

$$V_j + V_{k_{c,j}+1} > V_{j,j+1} \quad [20]$$

Finally, the number density of single pseudomolecules is calculated by

$$\frac{dN_1}{dt} = -N_1 \sum_{k=1}^{G_M} (1 + \delta_{1,k}) \Phi_{1,k} N_k \quad [21]$$

Equations [18], [19], and [21] are integrated over time for all size groups. The small number of size groups enables the model to simulate practical problems.

### B. PSG Method for Diffusion

Applying the PSG method to solid-state diffusion processes would seem to involve fewer rules than the particle collision method just presented because precipitate growth by diffusion involves gain or loss of only one individual pseudomolecule at a time. However, adding a single pseudomolecule to a particle rarely gives

enough particle growth to count it in the next larger size group. In addition, size groups  $j - 1$ ,  $j$ , and  $j + 1$  all influence the evolution of size group  $j$  number density during a given time interval. Thus, some knowledge of the particle distribution inside each size group is necessary, especially near the size group thresholds where the intergroup interaction occurs. This requires careful consideration of diffusion growth and dissociation both inside and between size groups.

All particles inside a size group  $j$  will still stay in group  $j$  even after a diffusion growth or dissociation event, except for those “border sizes” that fall on either side of the threshold sizes which define the neighboring size groups:  $n_j^L$  (closest to  $V_{j-1,j}$ ) and  $n_j^R$  (closest to  $V_{j,j+1}$ ). Size group  $j$  particles also can be generated if particles  $n_{j-1}^R$  from size group  $j - 1$  jump into size group  $j$  by diffusion growth or particles  $n_{j+1}^L$  from size group  $j + 1$  fall into size group  $j$  by dissociation. At the same time, size group  $j$  particles can be lost if particles  $n_j^R$  jump to size group  $j + 1$  by diffusion growth or particles  $n_j^L$  fall to size group  $j - 1$  by dissociation. These considerations are incorporated into a new PSG method, taking care to conserve mass, as follows:

$$\begin{aligned} \frac{dN_j}{dt} = & \frac{m_1}{m_j} \beta_j N_1 (N_j - n_j^R) - \frac{m_1}{m_j} \alpha_j A_j (N_j - n_j^L) \\ & + \frac{\text{ceil}(m_{j-1,j})}{m_j} \beta_{j-1}^R N_1 n_{j-1}^R + \frac{\text{floor}(m_{j,j+1})}{m_j} \alpha_{j+1}^L A_{j+1}^L n_{j+1}^L \\ & - \frac{\text{floor}(m_{j,j+1})}{m_j} \beta_j^R N_1 n_j^R - \frac{\text{ceil}(m_{j-1,j})}{m_j} \alpha_j^L A_j^L n_j^L \quad (j \geq 2) \end{aligned} \quad [22]$$

where  $n_j^L$  is the number density of those particles in size group  $j$  that fall into size group  $j - 1$  by losing one pseudomolecule, and  $n_j^R$  is the number density of those particles in size group  $j$  that jump into size group  $j + 1$  by gaining one pseudomolecule. Function  $\text{ceil}$  calculates the smallest integer that is not less than the given real number, and  $\text{floor}$  calculates for the largest integer that is not larger than the given real number. In Eq. [22], the first and second terms on the right-hand side account for the diffusion growth and dissociation inside size group  $j$ , and the third and fourth terms account for the generation of size group  $j$  particles by intergroup diffusion growth and dissociation of neighboring groups. The last two terms are for the loss of size group  $j$  particles because of the diffusion growth and dissociation of size group  $j$  particles themselves.

Single pseudomolecules are a special case because they comprise the only group that interacts with all other size groups. Thus, the new PSG method for diffusion uses the following population balance equation for  $j = 1$ :

$$\begin{aligned} \frac{dN_1}{dt} = & -N_1 \sum_{k=1}^{G_M} (1 + \delta_{1,k}) \beta_k (N_k - n_k^R) \\ & + \sum_{k=2}^{G_M} \alpha_k A_k (N_k - n_k^L) - N_1 \sum_{k=1}^{G_M} (1 + \delta_{1,k}) \beta_k^R n_k^R \\ & + \sum_{k=2}^{G_M} (1 + \delta_{2,k}) \alpha_k^L A_k^L n_k^L \end{aligned} \quad [23]$$

The diffusion growth rate  $\beta_j$  and dissociation rate  $\alpha_j$  of size group  $j$  particles needed to solve Eqs. [22] and [23] are calculated with Eqs. [7] through [9] using the characteristic (mean) radius given by Eq. [16]. The radius, diffusion growth rate, and dissociation rate for the border-sized particles are as follows:

$$r_j^L = (\text{ceil}(m_{j-1,j}))^{1/D_j} r_1, \quad r_j^R = (\text{floor}(m_{j,j+1}))^{1/D_j} r_1 \quad [24]$$

$$\beta_j^L = 4\pi D r_j^L, \quad \beta_j^R = 4\pi D r_j^R \quad [25]$$

$$\alpha_j^L = \frac{\beta_j^L N_{1,\text{eq}}}{A_j^L} \exp\left(\frac{2\sigma V_P}{R_g T} \frac{1}{r_j^L}\right), \quad \alpha_j^R = \frac{\beta_j^R N_{1,\text{eq}}}{A_j^R} \exp\left(\frac{2\sigma V_P}{R_g T} \frac{1}{r_j^R}\right) \quad [26]$$

The particle number densities for the border sizes  $n_j^L$  and  $n_j^R$  are estimated from a geometric progression approximation

$$n_j^L = n_{j-1}^C \left(\frac{n_j^C}{n_{j-1}^C}\right)^{\frac{\text{ceil}(m_{j-1,j}) - m_{j-1}}{m_j - m_{j-1}}}, \quad n_j^R = n_j^C \left(\frac{n_{j+1}^C}{n_j^C}\right)^{\frac{\text{floor}(m_{j,j+1}) - m_j}{m_{j+1} - m_j}} \quad [27]$$

To propagate particle growth, if  $n_j^L \neq 0$  and  $n_{j+1}^C = 0$ ,  $n_j^R$  is calculated by

$$n_j^R = n_j^L \left(\frac{n_j^C}{n_j^L}\right)^{\frac{\text{floor}(m_{j,j+1}) - \text{ceil}(m_{j-1,j})}{m_j - \text{ceil}(m_{j-1,j})}} \quad [28]$$

The particle number density at the center of each size group  $j$  is calculated by assuming two geometric progressions inside each size group

$$n_j^C = \frac{N_j}{\sum_{k=1}^{m_j - \text{ceil}(m_{j-1,j})} (1/q_j^L)^k + 1 + \sum_{k=1}^{\text{floor}(m_{j,j+1}) - m_j} (q_j^R)^k} \quad [29]$$

$$\text{with } q_j^L = \left(\frac{\bar{n}_j}{\bar{n}_{j-1}}\right)^{\frac{1}{m_j - m_{j-1}}}, \quad q_j^R = \left(\frac{\bar{n}_{j+1}}{\bar{n}_j}\right)^{\frac{1}{m_{j+1} - m_j}} \quad [30]$$

The average number density of size group  $j$  is calculated as

$$\bar{n}_j = \frac{N_j}{\text{floor}(m_{j,j+1}) - \text{ceil}(m_{j-1,j}) + 1} \quad [31]$$

Because the boundary ( $\text{ceil}$ ,  $\text{floor}$ ) and mean values of size groups are used directly and  $R_V$  is not explicitly found in these equations, this model is flexible to apply. This allows arbitrary size increments between groups in a single simulation, making it easy to improve accuracy with smaller  $R_V$  in size ranges of interest and to improve computation with larger  $R_V$  in other sizes. Alternatively,

the group sizes can be chosen to produce linearly spaced particle radius intervals, which are needed to compare with experiments.

## V. VALIDATION OF NEW PSG METHOD WITH TEST PROBLEMS

### A. Collision Test Problem

Saffman and Turner<sup>[25]</sup> suggested the turbulent collision frequency per unit volume of liquid medium to be

$$\Phi_{ij} = 1.3a(\varepsilon/v)^{1/2}(r_i + r_j)^3 \quad [32]$$

where  $\varepsilon$  is turbulent energy dissipation rate and  $v$  is kinematic viscosity. The empirical coefficient  $a$  was suggested by Higashitani *et al.*<sup>[70]</sup> and is assumed constant here. This model has been applied often to study inclusion agglomeration in liquid steel.<sup>[57,58,60–64,66]</sup> It is chosen here as a test problem to validate the collision model, using the complete integer-range equations in Section II as the exact solution.

Substituting into the dimensionless form of number density and time

$$n_i^* = n_i/n_0, t^* = 1.3a(\varepsilon/v)^{1/2}r_1^3n_0t \quad [33]$$

where  $n_0$  and  $r_1$  are the initial number density and the radius of single pseudomolecules. The initial condition is given by  $n_i^* = 1$  for  $i = 1$  and  $n_i^* = 0$  for  $i > 1$ . The size of the largest agglomerated particle is  $i_M = 12,000$ , so that accuracy within 0.05 pct error in the total particle volume is guaranteed up to  $t^* = 1$ . The boundary condition is always zero number density of the largest agglomerated particle (exact solution) and for the largest size group (PSG method). The Runge-Kutta-Gill method is applied for time integration with a time step of  $\Delta t^* = 0.0025$ . Smaller time step sizes produce negligible difference.

The total dimensionless number density of pseudomolecules and particles are defined as

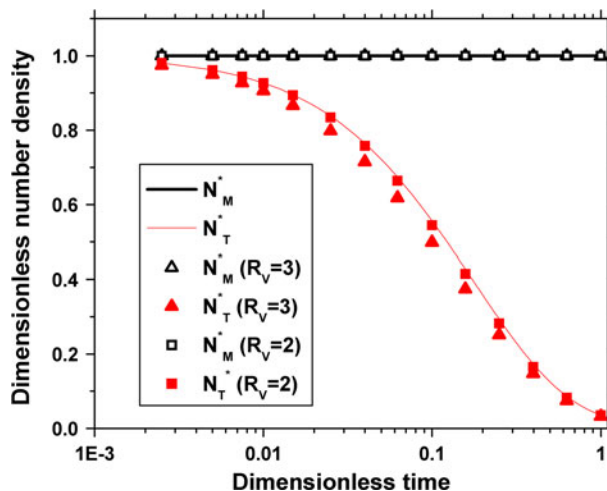


Fig. 2—Comparison of collision curve calculated by PSG method with exact solution for different  $R_V$ .

$$N_M^* = \sum_{i=1}^{i_M} i \cdot n_i^*, N_T^* = \sum_{i=1}^{i_M} n_i^* \quad \text{for exact solution}$$

$$N_M^* = \sum_{j=1}^{G_M} m_j \cdot N_j^*, N_T^* = \sum_{j=1}^{G_M} N_j^* \quad \text{for PSG method}$$

[34]

The mass balance requires  $N_M^*$  to be constant (equal to 1) through the entire calculation. Figure 2 shows the total particle volume is conserved for both the exact solution and PSG method. There is also good agreement between both cases for  $R_V = 3$  and  $R_V = 2$  for the total particle number density, which decreases with time because of agglomeration. Figure 3 shows that the evolution of the number densities of each size group with time from the PSG method also agrees reasonably with the exact solution for both  $R_V$  cases. With smaller  $R_V$ , the accuracy of the PSG method increases as expected.

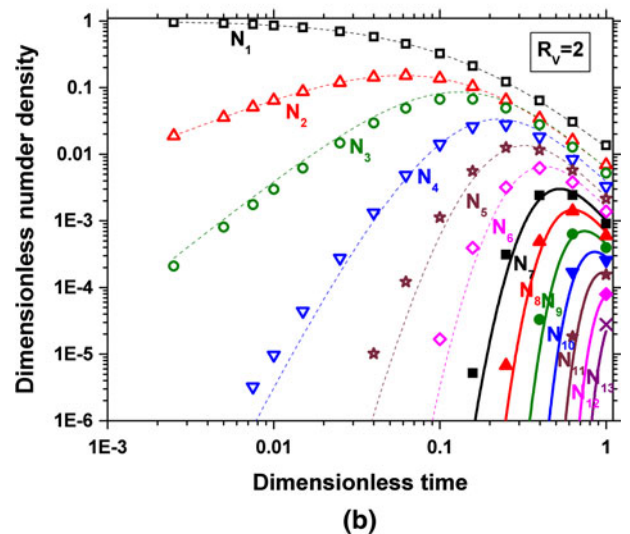
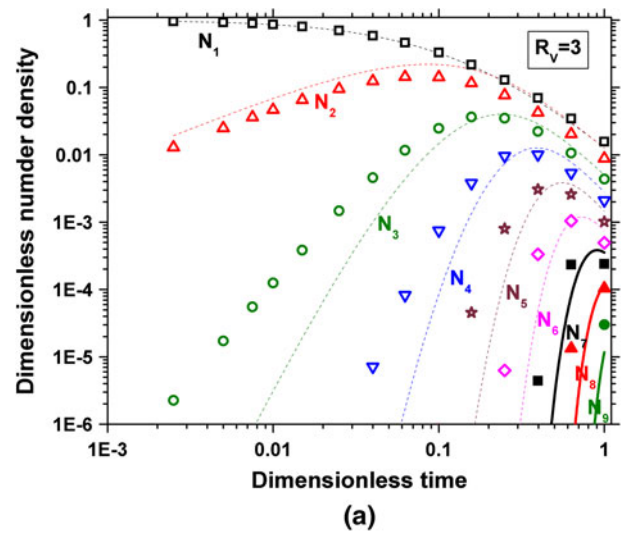


Fig. 3—Comparison of collision curve of each size group calculated by PSG method with exact solution for different  $R_V$ . (a)  $R_V = 3$  (b)  $R_V = 2$ .

**Table I. Comparison of Computational Cost for Test Problems**

	Collision ( $t^* = 1$ )			Diffusion ( $t^* = 10,000$ )		
	Exact	PSG ( $R_V = 2$ )	PSG ( $R_V = 3$ )	Exact	PSG ( $R_V = 2$ )	PSG ( $R_V = 3$ )
Storage	$i_M = 12,000$	$G_M = 16$	$G_M = 11$	$i_M = 50,000$	$G_M = 18$	$G_M = 13$
Computational time	$\sim 225$ h	$\sim 0.8$ s	$\sim 0.4$ s	$\sim 27$ h	$\sim 560$ s	$\sim 390$ s

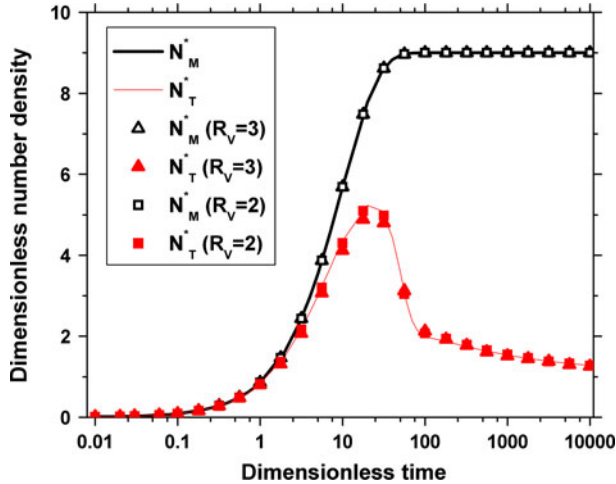


Fig. 4—Comparison of diffusion curves calculated by PSG method with exact solution for different  $R_V$ .

As time increases, collisions form large particles, leaving fewer smaller particles. For example, size group  $N_{10}$  in  $R_V = 2$  contains all particle sizes from 363 to 724 pseudomolecules, with a central size of 512 pseudomolecules. The number density of intermediate size groups increases at early times, reaches a maximum, and decreases at later times. The exact solution has limited maximum time because of its prohibitive computational cost. The tremendous computational efficiency of the PSG method is observed by examination of Table I.

**B. Diffusion Test Problem**

To validate the PSG diffusion model, a test problem is chosen where the total number density of single pseudomolecules in the system is produced by an isothermal first-order reaction<sup>[56]</sup>

$$n_s^*(t^*) = n_s(t^*)/n_{1,eq} = \sum_{i=1}^{i_M} i \cdot n_i^* = 9[1 - \exp(-0.1t^*)] \quad [35]$$

The number density of dissolved single pseudomolecules must be adjusted with time to match the increase of  $n_s^*$ . This increase with time can be interpreted as an increase in supersaturation caused by the decreasing temperature in a practical cooling process. The dimensionless terms are defined as

$$n_i^* = n_i/n_{1,eq}, t^* = 4\pi D_1 r_1 n_{1,eq} t \quad [36]$$

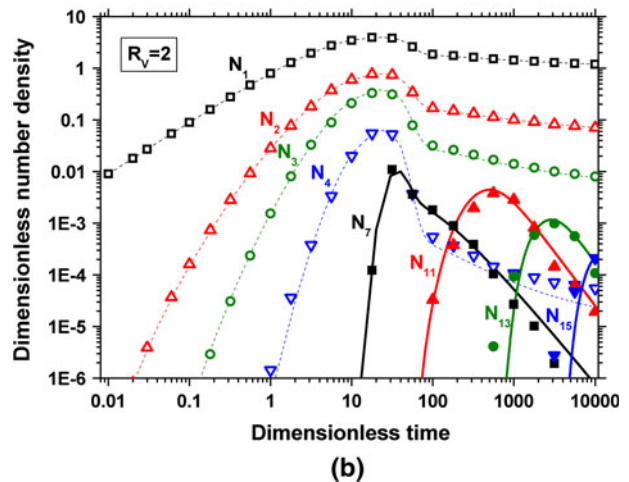
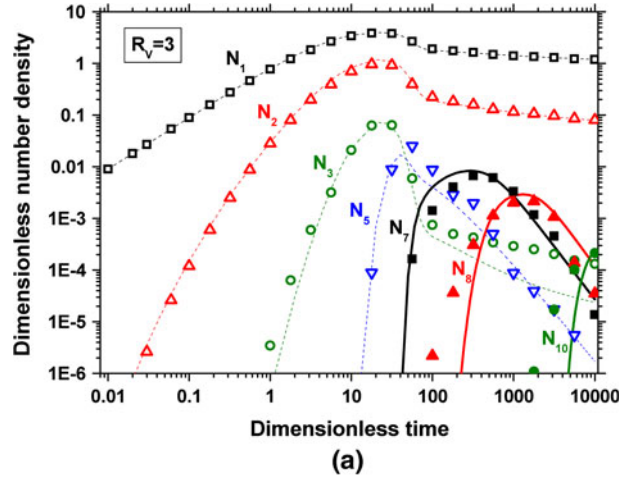


Fig. 5—Comparison of evolving numbers of each size group calculated by PSG diffusion method with exact solution for different  $R_V$ . (a)  $R_V = 3$  and (b)  $R_V = 2$ .

To calculate the dissociation rate in Eq. [9],  $2\sigma V_P / (R_g T r_1) = 3.488$ .<sup>[56]</sup> The initial condition is no particles, or  $n_i = 0$  for  $i \geq 1$ .

The boundary condition is always zero number density for the largest agglomerated particle (exact solution) or for the largest size group (PSG method). The maximum size of agglomerated particle is chosen as  $i_M = 50,000$  to ensure that mass conservation is satisfied up to  $t^* = 10,000$ . The explicit Runge-Kutta-Gill method was used for integration with time step size of  $\Delta t^* = 0.01$  chosen for accuracy. The maximum time



step for stability is roughly  $\Delta t^* = 0.04$  for both methods for this problem.

As shown in Figure 4, the total volume of particles is conserved for both the exact solution and the PSG method. This total increases with time and asymptotes at 9, according to Eq. [35]. The number density histories from all three cases also agree. Its behavior can be explained by examining Figure 5.

Figure 5 shows how the particle size distribution evolves because of the changing concentration gradients near particles of different size groups. At early times, all size group particles grow because of the driving force of increasing supersaturation. At later times, the results show Ostwald ripening. The large particles have low concentrations that tend to grow at the expense of smaller particles, which have high local concentrations, and eventually shrink. For example, the size group  $N_1$  (dissolved single pseudomolecules) reaches its peak and starts to decrease in number after  $t^* = 20$ . There is reasonable agreement for both total particle number density and number densities of each size group between the PSG method and the exact solution for both cases of  $R_V = 3$  and  $R_V = 2$ . The results for  $R_V = 2$  naturally match the exact solution more closely.

### C. Computation Times

The computation times for both test problems are listed in Table I. All the calculations are run with Matlab on Dell OPTIPLEX GX270 with P4 3.20GHz CPU and 2 GB RAM to enable a fair comparison. The computational cost decreases dramatically for the PSG method. It is interesting to note that the computation cost for the collision problem is proportional to  $i_M^2$  for the exact solution or  $G_M^2$  for the PSG method, whereas it is proportional to  $i_M$  or  $G_M$ , respectively, for the diffusion problem. Because the details of particle distribution inside the size groups must be captured to enable an accurate solution in a diffusion problem, the time saving is not as large. The savings increase exponentially with increasing maximum particle size. This is enough to make practical precipitation calculations possible, considering that less than 60 size groups cover particle sizes up to 100  $\mu\text{m}$  with constant  $R_V = 2$  for most nitrides and carbides in microalloyed steels.

## VI. PRACTICAL APPLICATIONS

When the PSG method is applied to model a real precipitation process, additional models are needed for the temperature history and for the mass concentrations of each element dissolved at equilibrium. The current work assumes the temperature history is given and uses a 13-element and 18-precipitate equilibrium precipitation model for microalloyed steels.<sup>[17]</sup> This model includes solubility limits for oxide, sulfide, carbide, and nitride precipitates in liquid, ferrite, and austenite; the influence of Wagner interaction on activities; and mass conservation of all elements during precipitation. Mutual solubility is incorporated for appropriate

precipitates with similar crystal structures and lattice parameters.

For a given steel composition and temperature history, the first step is to use the equilibrium model to compute the dissolved concentrations of every element at every temperature and to identify the critical element that restricts the number of single pseudomolecules available to form the precipitate of interest, as a function of time. The initial condition starting from the liquid state is complete dissolution with the number density of single pseudomolecules,  $N_1(t = 0)$ , equal to the total number density  $n_s$  of the precipitate of interest. For a given steel composition containing  $M_0$  of element  $M$  and  $X_0$  of element  $X$ , then  $n_s$  for precipitate  $M_xX_y$  is

$$n_s = \min\left(\frac{M_0 \rho_{\text{steel}}}{100 x A_M} N_A, \frac{X_0 \rho_{\text{steel}}}{100 y A_X} N_A\right) \quad [37]$$

where  $A_M$  and  $A_X$  are the atomic masses of elements  $M$  and  $X$ , and  $\rho_{\text{steel}}$  is the density of the steel matrix (7500  $\text{kg m}^{-3}$ ). All other particle sizes have zero number densities.

Sometimes, such as after a solution treatment, some of the initial processing steps from the liquid state can be ignored or replaced with a measured initial distribution. Because the current model can handle only one precipitate, the initial composition must be the dissolved concentration available for that precipitate after taking away the other precipitates that form first. For example, in the cases involving nitride AlN formation, a new Al concentration is used after subtracting the more stable oxide  $\text{Al}_2\text{O}_3$ .

The equilibrium number density of single pseudomolecules of the precipitate in the steel  $n_{1,\text{eq}}$  is calculated from the dissolved mass concentrations  $[M]$  and  $[X]$  at equilibrium in the same way

$$n_{1,\text{eq}} = \min\left(\frac{[M] \rho_{\text{steel}}}{100 x A_M} N_A, \frac{[X] \rho_{\text{steel}}}{100 y A_X} N_A\right) \quad [38]$$

Although the current work only calculates size distributions for a single precipitate, other alloys may affect the results by forming other precipitates that change the equilibrium dissolved concentrations of the elements in the precipitate of interest. These effects are included through the equilibrium model, in addition to Wagner interactions.<sup>[17]</sup>

The PSG kinetic model is then run, knowing the history of the equilibrium number density of single pseudomolecules of the chosen precipitate. The diffusion coefficients and dissociation rates in Eqs. [7] through [9] and [24] through [26] are updated for each time step according to the temperature history. This model calculates how the particle size distribution evolves with time.

When running the PSG model, time steps must be large enough to enable reasonable computation cost, while avoiding stability problems resulting from dissociation exceeding diffusion growth. Thus, the implicit Euler scheme is adopted here to integrate Eqs. [22] through [31] through time

$$\begin{aligned}
& \left[ 1 + \Delta t \left( \frac{m_1}{m_j} \alpha_j A_j + \frac{\text{floor}(m_{j,j+1})}{m_j} \beta_j^R N_1^{i+1} + \frac{\text{ceil}(m_{j-1,j})}{m_j} \alpha_j^L A_j^L \right) \right] \\
& \times N_j^{i+1} = N_j^i + \Delta t \left[ \frac{m_1}{m_j} \beta_j N_1^{i+1} (N_j^{i+1} - n_j^R) + \frac{m_1}{m_j} \alpha_j A_j n_j^L \right. \\
& + \frac{\text{ceil}(m_{j-1,j})}{m_j} \beta_{j-1}^R N_1^{i+1} n_{j-1}^R + \frac{\text{floor}(m_{j,j+1})}{m_j} \alpha_{j+1}^L A_{j+1}^L n_{j+1}^L \\
& + \frac{\text{floor}(m_{j,j+1})}{m_j} \beta_j^R N_1^{i+1} (N_j^{i+1} - n_j^R) \\
& \left. + \frac{\text{ceil}(m_{j-1,j})}{m_j} \alpha_j^L A_j^L (N_j^{i+1} - n_j^L) \right] \quad (j \geq 2) \quad [39]
\end{aligned}$$

where  $i$  is the time-step index. This implicit scheme allows over  $10^4$ -fold increase in time step size, compared with the original explicit scheme, for realistic precipitate/matrix interfacial energies  $\sim 0.5 \text{ J/m}^2$ . The preceding equation system is solved with the iterative Gauss-Seidel method until the largest relative change of  $N_j^{i+1}$  converges to within less than  $10^{-5}$  between two iterations. The upper limits of  $n_j^L$  and  $n_j^R$  are  $N_j^{i+1}$  and are evaluated at each iteration. Although this scheme is stable for any time step size, its accuracy may deteriorate if the time step is too large. Thus, a reasonable time step must be chosen where results stay almost the same with a smaller time step.

Having validated mass conservation with test problems, the number density of single pseudomolecules is then computed as follows to save computation time relative to Eq. [23]:

$$N_1^{i+1} = n_s - \sum_{j=2}^{G_M} m_j N_j^{i+1} \quad [40]$$

To postprocess the results, the total number density of precipitate particles  $n_p$ , fraction precipitated  $f_p$ , mean precipitate particle radius  $\bar{r}_p$ , and precipitate volume fraction  $\phi_p$  are computed from the number densities as follows:

$$n_p = \sum_{j=G_T}^{G_M} N_j \quad [41]$$

$$f_p = \frac{\sum_{j=G_T}^{G_M} m_j N_j}{n_s} \quad [42]$$

$$\bar{r}_p = \frac{\sum_{j=G_T}^{G_M} r_j N_j}{n_p} \quad [43]$$

$$\phi_p = f_p \frac{n_s}{n_s - n_{1,\text{eq}}} \frac{\rho_{\text{steel}}}{\rho_p} \frac{w_p^e}{100} \quad [44]$$

where size group  $G_T$ , which contains particles just larger than a “truncating” threshold radius  $r_{T-1,T}$ , is introduced to define the split between “dissolved” and measurable particles. This parameter must be introduced because all experimental techniques have resolution limits, whereas

the current PSG model simulates particles of all sizes including single pseudomolecules.  $\rho_p$  is the density of the precipitate phase, and  $w_p^e$  is the mass concentration of precipitate at equilibrium (wt pct).

The complete PSG model is applied in this study to two different example precipitate systems, where measurements are available for validation.

### A. Precipitated Fraction for Isothermal AlN Precipitation

The first validation problem for the PSG diffusion model was to simulate the isothermal precipitation of AlN in a 0.09 pct C, 0.20 pct Si, 0.36 pct Mn, 0.051 pct Al, and 0.0073 pct N steel for the experimental conditions measured by Vodopivec.<sup>[71]</sup> Specimens were solution treated at 1573 K (1300 °C) for 2 hours, “directly” cooled to the precipitation temperature of 1113 K or 973 K (840 °C or 700 °C), aged for various times, and quenched. The AlN content in steel was measured using the Beeghly method.<sup>[72]</sup>

The initial experimental measurements (zero and short aging times) report 6.4 pct of the total N ( $N_0 = 0.0073$  pct) precipitated as AlN, perhaps because the cooling stages were not fast enough. The final precipitated amounts of nitrogen as AlN do not reach the predictions of the equilibrium model, even after long holding times, when the precipitated fraction becomes nearly constant. This might be because N was consumed into other types of nitrides. Thus, the measurements are normalized to zero at zero aging time, and  $(N_0 - [N])/N_0$  at long times.

As shown in Figure 6, the equilibrium model<sup>[17]</sup> predicts AlN to start forming at 1509 K (1236 °C), and the equilibrium dissolved concentration of nitrogen in steel is  $\sim 0.00022$  wt pct at 1113 K (840 °C) and  $\sim 0.0000031$  wt pct at 973 K (700 °C). A sharp decrease of equilibrium dissolved aluminum concentration can be

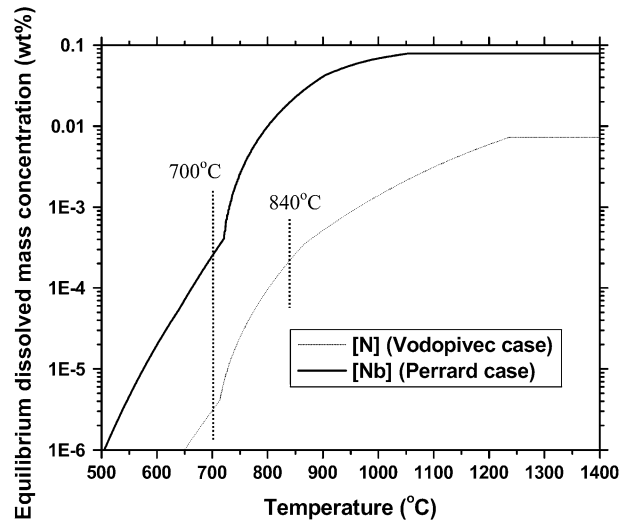


Fig. 6—Calculated equilibrium dissolved mass concentration of N for Vodopivec case<sup>[71]</sup> and Nb for Perrard case<sup>[79]</sup> showing aging test temperatures.

observed over the  $\gamma \rightarrow \alpha$  phase transformation, 1138 K to 988 K (865 °C to 715 °C), because of the lower solubility limit of AlN in ferrite predicted by the equilibrium model.

Isothermal precipitation simulations of 1 hour at 973 K (700 °C) and 3 hours at 1113 K (840 °C) were run, neglecting the cooling histories before and after, which were not clearly reported. The molar volume of AlN is  $12.54 \times 10^{-6} \text{ m}^3/\text{mol}$ <sup>[73]</sup> and the diffusion coefficient of Al in steel  $D_{\text{Al}}(\text{m}^2/\text{s})$  is taken as  $2.51 \times 10^{-4} \exp(-253400/RT)$ <sup>[74]</sup> in austenite, and  $0.3 \times 10^{-2} \exp(-234500/RT)$ <sup>[73]</sup> in ferrite. The interfacial energies for these two precipitation temperatures are calculated in the appendix, where the value is observed to be 10pct higher at 973 K (700 °C) in ferrite than at 1113 K (840 °C) in austenite. The number densities of precipitate particles are calculated based on the nitrogen concentration because this element is insufficient when reacting with aluminum to form AlN for this steel composition. Constant  $R_V = 2$  and 32 size groups are used in the simulation, which covers particle radii up to approximately 200 nm. The time step is 0.001 seconds with  $\sim 1000$  decreasing to  $\sim 100$  iterations required within each time step for convergence of the implicit method with Gauss-Seidel solver. Because it has been suggested that the Beeghly technique cannot detect fine precipitate particles which could pass through the filter,<sup>[75,76]</sup> the truncating precipitate radius is set to 2.0nm in the simulation to match the measurements.

The predicted AlN precipitate fractions are shown and compared with experimental measurements in Figure 7. Reasonable matches are shown at both temperatures. The calculation verifies the experimental observation of much faster precipitation in ferrite than in austenite because of the lower solubility limit of AlN and the faster diffusion rate of aluminum in ferrite than in austenite. The disagreement could be to the result of AlN precipitation on the grain boundaries because the physical properties assumed in the simulation are based

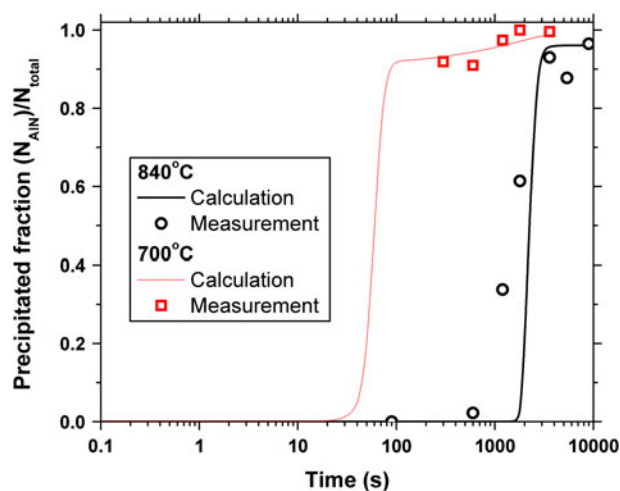


Fig. 7—Calculated and measured precipitated fraction of AlN in 0.051 wt pct Al-0.0073 wt pct N steel during isothermal aging at 1113 K and 973 K (840 °C and 700 °C) (experimental data from Vodopivec<sup>[71]</sup>).

on homogeneous precipitation in the steel matrix. The same mismatch in predicting AlN precipitation has been found and discussed by other researchers.<sup>[77,78]</sup>

## B. Size Distribution for Isothermal Niobium Precipitation

The second validation problem is to simulate the size distribution of niobium precipitate particles in steel containing 0.079 pct Nb, 0.011 pct C, 0.001 pct N, 0.002 pct Mn, 0.0023 pct S, 0.001 pct P, 0.006 pct Al, and 0.0013 pct O to compare the PSG simulation predictions with the niobium precipitate distribution measured in ferrite.<sup>[79]</sup> The alloy was vacuum induction melted, cast into ingots, and hot rolled from 50 mm to 5 mm thickness. After homogenization at 1623 K (1350 °C) for 45 minutes, the specimens were quenched rapidly to an aging temperature of 973 K (700 °C) and held for various times. Small-angle neutron scattering (SANS) and transmission electron microscopy (TEM) were used to measure precipitate size.

The equilibrium calculation in Figure 6 predicts that the niobium precipitates in this steel first become stable at 1327 K (1054 °C), and the equilibrium dissolved mass concentration of the niobium is 0.0002506 wt pct at 973 K (700 °C).<sup>[17]</sup> For the PSG precipitation simulation, the diffusion coefficient of Nb in ferrite is taken as  $D_{\text{Nb}}(\text{m}^2/\text{s}) = 50.2 \times 10^{-4} \exp(-252000/RT)$ ,<sup>[80]</sup> the molar volume of NbC is  $13.39 \times 10^{-6} \text{ m}^3/\text{mol}$ ,<sup>[73]</sup> the density of NbC is  $7.84 \times 10^3 \text{ kg/m}^3$ ,<sup>[73]</sup> and the interfacial energy is calculated in the appendix. The composition of the niobium precipitates in the simulation was regarded as  $\text{NbN}_{0.08}\text{C}_{0.80}$ , according to the predictions of the equilibrium model,<sup>[17]</sup> for this steel, where pct C > pct N. This composition agrees with the experimental observation of “niobium carbide” precipitates and the nonstoichiometric ratio of  $\text{NbC}_{0.87}$  measured in other work.<sup>[81]</sup> Lacking data for this complex Nb precipitate, property data were taken for NbC, which are believed to be similar, as the lattice constants of NbC and  $\text{NbC}_{0.87}$  differ by only  $\sim 0.2$  pct.<sup>[82]</sup>

To compare with the experimental measurements,  $R_V$  was set equal to 2 for particles with radius smaller than 0.3 nm and larger than 10 nm, and these values varied to give constant 0.2-nm size groups for 0.3 to 8.5 nm, and 0.5 nm size groups for 8.5 to 10 nm. A total of 50 size groups were used to model particle sizes up to 20 nm to cover the largest particle observed in the experiments. The implicit time step was 0.01 seconds, with less than 10 iterations needed for convergence at most times, resulting in  $\sim 2.5$  days of total CPU time on a 3.20 GHz processor PC for the 600,000 seconds (7 days) simulation. Rapid quenching from solution treatment to aging temperature and from aging to ambient is assumed, so only an isothermal simulation at 973 K (700 °C) was performed.

Predicted evolutions of precipitate mean size, size distribution, and volume fraction results from the PSG simulation are shown in Figures 8 and 9, and were compared with available measurements.<sup>[79]</sup> Because the many dislocations in the matrix from the prior

deformation may relax the lattice mismatch and decrease the interface energy, they become favored locations for precipitation. Figure 8 shows that lowering

the interface energy to  $0.3 \text{ J/m}^2$  and choosing a truncating radius of  $0.7 \text{ nm}$  gives the best match of both mean precipitate size and volume fraction with the SANS measurements. These results also indicate that decreasing interface energy makes the capillary effect smaller, which makes large particles more difficult to grow, so a finer precipitate size and slower precipitation are predicted. All volume fraction curves eventually reach the equilibrium value of  $0.084 \text{ pct}$  for aging at  $973 \text{ K}$  ( $700 \text{ }^\circ\text{C}$ ). These calculations of decreasing interface energy are qualitatively consistent with the experimental observations of deformation-induced nanosized Cu precipitation.<sup>[83]</sup> Increasing the truncating radius from  $0.5 \text{ nm}$  to  $0.7 \text{ nm}$  significantly delays the apparent precipitation, although it has only minor influence on the calculated mean precipitate size and only during the initial stage of precipitation.

The simulation results with the adjusted interface energy  $0.3 \text{ J/m}^2$  are compared with the normalized TEM measured particle size distribution/volume number frequency in ferrite at 300 minutes in Figure 9. The predicted mean radius of Nb precipitate particles of  $1.93 \text{ nm}$  compares closely with the measured  $1.82 \text{ nm}$ , and the particle size distributions also match reasonably. The simulated size distribution is missing the measured tail of large particles, however. This is likely because of easier nucleation and higher diffusion at the grain boundaries, segregated regions, and other locations in the steel microstructure, where larger precipitates can form locally in the real samples. In addition, the observed particles in TEM imaging have irregular aspect ratio  $\sim 2.3$ ,<sup>[79]</sup> which differs from the spherical assumption of the model and suggests nonisotropic properties.

The calculated evolution of the size distribution of the Nb particles is depicted in Figure 10. Each curve has the same characteristic shape, which evolves with time. The number densities decrease with increasing particle size to a local minimum, increase to a peak, and finally decrease to zero. With increasing time, the number density of single (dissolved) pseudomolecules decreases from the large initial value  $n_s$  that contains all of the particles to the small equilibrium value  $n_{1,\text{eq}}$ . Small

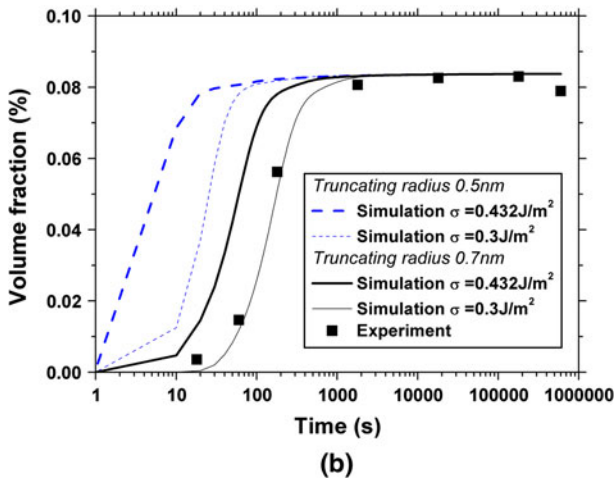
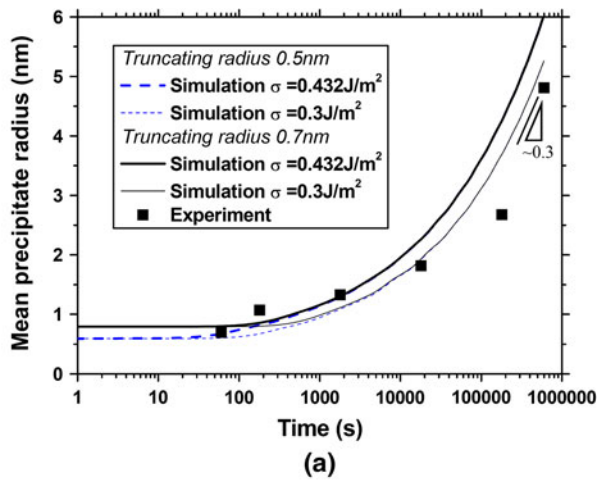


Fig. 8—Comparison of calculated and SANS measured niobium precipitation during isothermal aging at  $973 \text{ K}$  ( $700 \text{ }^\circ\text{C}$ )<sup>[79]</sup> (a) Mean precipitate radius  $\bar{r}_p$  and (b) volume fraction precipitated  $\varphi_p$ .

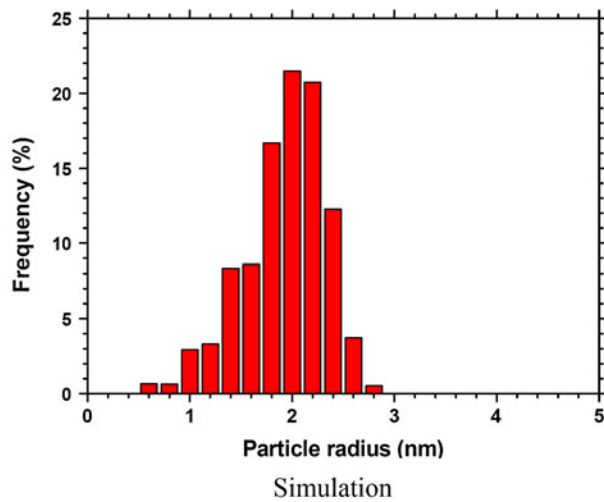
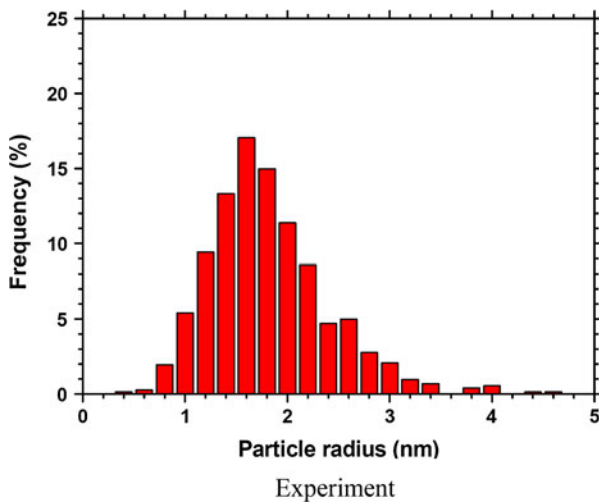


Fig. 9—Normalized size distribution of niobium particles simulated compared with TEM measurements at  $18,000 \text{ s}$  ( $300 \text{ min}$ )<sup>[79]</sup>.

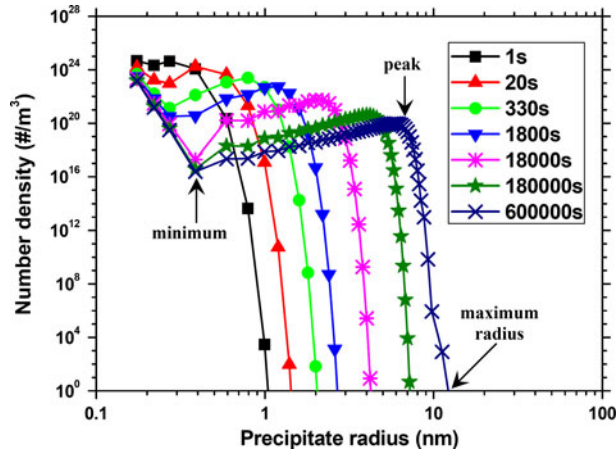


Fig. 10—Calculated size distributions of niobium precipitate particles.

particles in the first few size groups are unstable, as the chance of gaining pseudomolecules is less than that of losing pseudomolecules because of the high surface curvature. Thus, their number densities decrease with size because of the decreasing chance of a larger unstable embryo of pseudomolecules coming together from the simulated process of random thermal diffusion. With increasing size above the critical size, pseudomolecule attachment increasingly exceeds dissolution, so these stable particles grow increasingly faster and become larger. Very large particles are rare simply because of insufficient growth time.

The entire size distribution grows larger with time. Except for the small unstable embryos that decrease in number, all other particle sizes increase in number during this period. The maximum particle radius increases from 1.4 nm at 20 seconds to 2.0 nm at 330 seconds, whereas the most common size (peak number density) increases from 0.4 nm to 0.8 nm.

After this initial growth stage, single pseudomolecules approach the equilibrium concentration. Smaller particles then decrease slowly in number because of dissolution, which provides single pseudomolecules for the slow growth of large particles. This is the particle coarsening or “Ostwald ripening” stage. This final precipitation stage is estimated to begin at ~330 seconds, based on the maximum total number of particles larger than 0.7 nm, shown in Figure 11. This time matches with the decrease in slope of precipitated volume fraction with time that is both predicted and measured in Figure 8(b). The precipitate size evolution after 100,000 seconds roughly follows the law of  $\bar{r}_p \propto t^{0.3}$  in Figure 8(a), which agrees with the value of 1/3 from classic LSW coarsening theory.<sup>[33,34]</sup> As larger particles grow and smaller particles shrink during coarsening, the total number of particles decreases. This corresponds to the evolution of critical radius, included in Figure 11. Starting smaller than the mean size, the critical size increases with time to approach the mean, as supersaturation decreases toward 1 at equilibrium.

## VII. DISCUSSION

The calculated precipitated fraction of aluminum nitride and the mean size, volume fraction, and size

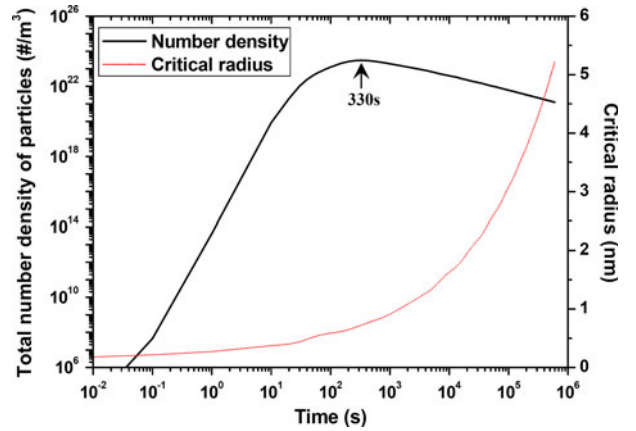


Fig. 11—Calculated number density and critical radius of niobium precipitate particles.

distribution of niobium carbide particles all match well with experiments. This is significant because no fitting parameters are introduced in this model. The match is governed by the equilibrium dissolved concentration (supersaturation) calculated from the equilibrium model and the choice of the physical parameters: diffusion rate and interfacial energy.

The model results quantify and provide new insight into the classic stages of precipitate nucleation, growth, and coarsening. For example, a critical radius  $r_c$  can be obtained by setting  $\beta_i n_{1i} = \alpha_i A_i$ , which means that the rate of particle growth from the diffusion of single pseudomolecules to the surface exactly matches the rate of particle shrinking by dissociation, and from Eqs. [8] and [9], leads to

$$r_c = \frac{2\sigma V_p}{R_g T \ln(n_1/n_{1,eq})} \quad [45]$$

At this critical size, the surface concentration of pseudomolecules  $n_{1i}$  equals that at the far-field  $n_1$ . Although this relation holds at any time, it is consistent with classic nucleation theory, which balances the decrease in volumetric free energy  $\Delta G_V$  in forming a spherical nucleus with the energy increase to form the new interface  $\sigma$  and gives the critical radius for a stable particle  $r_c$  of<sup>[84]</sup>

$$r_c = \frac{2\sigma}{\Delta G_V} \quad [46]$$

where  $\Delta G_V$  for a single precipitate system is:

$$\Delta G_V = \frac{R_g T}{V_p} \ln \Pi \quad [47]$$

where  $\Pi$  is the time-dependent supersaturation, which can be interpreted as  $n_1/n_{1,eq}$  in the current model. The same trends of critical radius in Figure 11 are observed with classic precipitation models.<sup>[40]</sup> The current PSG method is more general, however, as the precipitation evolves naturally according to the time-varying local concentration gradients and cooling conditions.

The main purpose of this work is to present a numerical method that offers a fundamental framework to model precipitation kinetics over the complete size range from atomic-scale pseudomolecules to realistic coarsened inclusion particles. This new PSG methodology could be extended to other models, such as cluster dynamics, where it could significantly reduce the single cluster size and expand the simulation size range with reasonable computational cost.

The results presented here are only approximate because homogeneous nucleation of only one type of precipitate was simulated, instead of the many that actually form in steel, and only the physical properties of the matrix phase were adopted. These are not fundamental limitations of the method, however. Competition between the different precipitates for the alloy elements, such as different nitrides consuming nitrogen, causes inaccuracies that can be addressed by generalizing the current model to handle multiple precipitates. Such an enhanced multiphase precipitate model is also needed to account for previously formed precipitates that act as heterogeneous nucleation sites for new precipitates of different composition. Heterogeneous nucleation also needs consideration of grain-boundary and dislocation effects on the interfacial energy.

Many other improvements are needed to transform this new PSG-based precipitation model into an accurate predictive tool for commercial metals-processing applications. Microsegregation changes the alloy composition at grain boundaries, where increased vacancy concentration also increases diffusion rates.<sup>[80]</sup> The interfacial energy should evolve with temperature and time according to the microstructure, precipitate composition and size, local strain field around the precipitate, coherency of the interface, and macroscopic deformation. Strain and deformation influence precipitation kinetics by changing the microstructure and lowering interfacial energy,<sup>[30,85]</sup> which possibly increases the nucleation and growth rate,<sup>[86,87]</sup> leading to a much finer particle size distribution.<sup>[87,88]</sup> These and other effects on precipitation behavior should be addressed in future improvements to this model.

## VIII. CONCLUSIONS

1. The PSG population-balance method for modeling particle collision was derived for an arbitrary choice of size ratio  $R_V$  and good agreement has been verified with exact solutions.
2. A new, efficient PSG population-balance method for diffusion-controlled particle growth has been developed. The method features geometrically-based thresholds between each size group, reasonable estimates of border values in order to accurately include intra-group diffusion, corresponding accurate diffusion between size groups, and an efficient implicit solution method to integrate the equations.
3. Results from this PSG method match the exact solution for diffusion test problems very well.
4. For a given size range, the PSG method costs exponentially less computational time than the original

population balance calculation. This enables accurate and realistic modeling of nonequilibrium precipitation processes at reasonable computational cost.

5. The new PSG method can simulate particle incubation, nucleation, growth, and coarsening from collision and diffusion over a wide size range, with no explicit laws or fitting parameters for these stages. Accuracy of the method increases with decreasing  $R_V$  as more size groups are used to cover the given particle size range.
6. The new PSG method has been applied to two realistic validation problems. The computed fraction of aluminum nitride precipitated and the mean size, volume fraction, size distributions of niobium carbide precipitated show encouraging agreement with previous experimental measurements in microalloyed steel. Precipitation in ferrite is found to be greatly accelerated as demonstrated the lower solubility limit and higher diffusion rate of these precipitates in this phase.
7. The predicted time evolution of the particle size distribution exhibits trends of critical size, number, and slope that are consistent with classic nucleation, growth, and coarsening theories.
8. The new PSG method presented here offers a versatile and efficient framework for the development of realistic models of nonequilibrium precipitation behavior during metals processes, such as the continuous casting of steel, for arbitrary temperature histories. To become useful, future work needs to incorporate other important effects, such as multiple precipitate phases, different behaviors at the grain boundaries and matrix, interdendritic and grain-boundary segregation, and other microstructural effects. Furthermore, better experiments and fundamental models are needed to quantify the model parameters (diffusion coefficients and interfacial energies), which should evolve with temperature and time according to the microstructure, local strain field, coherency of the interface, and macroscopic deformation.

## ACKNOWLEDGMENT

The authors thank the Continuous Casting Consortium at the University of Illinois at Urbana-Champaign and the National Science Foundation (Grant CMMI-0900138) for support of this project.

## APPENDIX: CALCULATION OF INTERFACIAL ENERGY

According to Turnbull<sup>[89]</sup> and Liu and Jonas,<sup>[90]</sup> the interfacial energy consists of two parts: a chemical part ( $\sigma_c$ ) and a structural part ( $\sigma_{st}$ ), so that

$$\sigma = \sigma_c + \sigma_{st} \quad [A1]$$

The chemical interfacial energy is estimated from the difference between the energies of bonds broken in the separation process and of bonds made in forming the interface, with only the nearest neighbors considered. As given by Russell<sup>[36]</sup>

$$\sigma_c = \frac{\Delta E_0 N_s Z_s}{N_A Z_l} (X_P - X_M)^2 \quad [\text{A2}]$$

where  $\Delta E_0$  is the heat of solution of precipitates in a dilute solution in the matrix,  $N_s$  is the number of atoms per unit area across the interface,  $Z_s$  is the number of bonds per atom across the interface,  $Z_l$  is the coordinate number of nearest neighbors within the precipitate crystal lattice, and  $X_P$  and  $X_M$  are the molar concentrations of the precipitate-forming element in the precipitate (P) and matrix (M) phase, respectively.  $\Delta E_0$  is estimated to equal  $-\Delta H$ , the heat of formation of the precipitate.  $X_P = 0.5$  and  $X_P \gg X_M$ .

Van Der Merwe<sup>[91]</sup> presented a calculation of structural energy for a planar interface. When the two phases have the same structure and orientation but different lattice spacing, the mismatch may be accommodated by a planar array of edge dislocations. Including the strain energy in both crystals,  $\sigma_{st}$  is given as

$$\sigma_{st} = \frac{\mu_l \bar{c}}{4\pi^2} \left\{ 1 + \beta - (1 + \beta^2)^{1/2} - \beta \ln \left[ 2\beta(1 + \beta^2)^{1/2} - 2\beta^2 \right] \right\} \quad [\text{A3}]$$

$$\text{with } \frac{2}{\bar{c}} = \frac{1}{c_M^e} + \frac{1}{c_P^e}, \quad \beta = 2\pi\delta \frac{\lambda_+}{\mu_l}, \quad \frac{2}{\mu_l} = \frac{1}{\mu_M} + \frac{1}{\mu_P},$$

$$\delta = \frac{2|c_M^e - c_P^e|}{c_M^e + c_P^e}, \quad \frac{1}{\lambda_+} = \frac{1 - \nu_M}{\mu_M} + \frac{1 - \nu_P}{\mu_P} \quad [\text{A4}]$$

where  $c_M^e$  and  $c_P^e$  are the nearest-neighbor distance across the interface, which are estimated from the lattice parameters  $c_M$ ,  $c_P$ , and interface orientations;  $\bar{c}$  is the spacing of a reference lattice across the matrix/precipitate interface;  $\mu_M$ ,  $\mu_P$ , and  $\mu_l$  are shear moduli in the matrix (M), precipitate (P), and interface (I), respectively;  $\nu_M$  and  $\nu_P$  are Poisson's ratios; and  $\delta$  is the lattice misfit across the interface.

The crystallographic relationships between the AlN (hexagonal close packed [hcp]), NbC (face centered cubic [fcc]), and steel matrix austenite phase (fcc) or ferrite phase (base-centered cubic [bcc]) are chosen as  $(100)_{\text{NbC}} // (100)_{\alpha\text{-Fe}}$ ,<sup>[92]</sup>  $(0001)_{\text{AlN}} // (111)_{\gamma\text{-Fe}}$ ,<sup>[93,94]</sup> and  $(0001)_{\text{AlN}} // (110)_{\alpha\text{-Fe}}$ .<sup>[95]</sup>

The physical properties used in the calculation are  $-\Delta H_{\text{AlN}} (\text{KJ/mol}) = 341.32 - 4.98 \times 10^{-2} T - 1.12 \times 10^{-6} T^2 - 2813/T$ ,<sup>[96]</sup>  $-\Delta H_{\text{NbC}} (\text{KJ/mol}) = 157.76 - 4.54 \times 10^{-2} T - 3.84 \times 10^{-6} T^2$ ,<sup>[97]</sup>  $\mu_{\gamma\text{-Fe}} (\text{GPa}) = 81[1 - 0.91(T - 300)/1810]$ ,<sup>[98]</sup>  $\nu_{\gamma\text{-Fe}} = 0.29$ ,<sup>[99]</sup>  $c_{\gamma\text{-Fe}} (nm) = 0.357$ ,<sup>[73]</sup>  $\mu_{\alpha\text{-Fe}} (\text{GPa}) = 69.2[1 - 1.31(T - 300)/1810]$ ,<sup>[98]</sup>  $\nu_{\alpha\text{-Fe}} = 0.29$ ,<sup>[99]</sup>  $c_{\alpha\text{-Fe}} (nm) = 0.286$ ,<sup>[73]</sup>  $\mu_{\text{AlN}} (\text{GPa}) = 127$ ,<sup>[100]</sup>  $\nu_{\text{AlN}} = 0.23$ ,<sup>[100]</sup>  $a_{\text{AlN}} (nm) = 0.311$ ,  $c_{\text{AlN}} (nm) = 0.497$ ,<sup>[73]</sup>  $\mu_{\text{NbC}} (\text{GPa}) = 134[1 - 0.18(T - 300)/3613]$ ,<sup>[98]</sup>  $\nu_{\text{NbC}} = 0.194$ ,<sup>[98]</sup>  $c_{\text{NbC}} (nm) = 0.446$ .<sup>[73]</sup>

For  $\gamma\text{-Fe}$  (111) plane,  $Z_s^{\gamma\text{-Fe}} = 3$  and  $N_s^{\gamma\text{-Fe}} = 4/(\sqrt{3}c_{\gamma\text{-Fe}}^2)$ . For  $\alpha\text{-Fe}$ , (110) plane  $Z_s^{\alpha\text{-Fe}} = 4$ ,  $N_s^{\alpha\text{-Fe}} = \sqrt{2}/c_{\alpha\text{-Fe}}^2$ , (100) plane  $Z_s^{\alpha\text{-Fe}} = 4$ , and  $N_s^{\alpha\text{-Fe}} = 1/c_{\alpha\text{-Fe}}^2$ . For both fcc and hcp precipitate structures,  $Z_l = 12$ . The calculated interfacial energy decreases slightly as temperature increases and also decreases for NbC (relative to AlN) because of lower heat of formation. The values used in the current simulations are

$$\sigma_{\text{AlN}}^{\gamma\text{-Fe}} (840 \text{ }^\circ\text{C}) = 0.908 \text{ J/m}^2$$

$$\sigma_{\text{AlN}}^{\alpha\text{-Fe}} (700 \text{ }^\circ\text{C}) = 0.997 \text{ J/m}^2$$

$$\sigma_{\text{NbC}}^{\alpha\text{-Fe}} (700 \text{ }^\circ\text{C}) = 0.432 \text{ J/m}^2$$

## NOMENCLATURE

$a$	empirical coefficient for turbulence collision
$c_M, c_P$	lattice parameter of the matrix and precipitate phase (m)
$c_M^e, c_P^e$	nearest-neighbor distance across the interface for matrix and precipitate phase (m)
$f$	transformed fraction in phase transformation
$f_P$	particle (or mass) fraction precipitated (relative to 100pct at zero dissolved)
$i_M$	number of pseudomolecules for the largest agglomerated particle in simulation
$m_j$	number of pseudomolecules contained in PSG volume $V_j$
$m_{j-1,j}$	number of pseudomolecules contained in PSG threshold volume $V_{j-1,j}$
$n$	Avrami exponent in KJMA model
$n_0$	initial total number density of single pseudomolecules for collision problem ( $\# \text{ m}^{-3}$ )
$n_{1,\text{eq}}$	equilibrium concentration of dissolved single pseudomolecules for diffusion problem ( $\# \text{ m}^{-3}$ )
$n_{1i}$	equilibrium concentration of single pseudomolecules at surface of size $i$ particles ( $\# \text{ m}^{-3}$ )
$n_i$	number density of size $i$ particles ( $\# \text{ m}^{-3}$ )
$n_P$	total number density of precipitate particles ( $\# \text{ m}^{-3}$ )
$n_s$	released number density of single pseudomolecules for diffusion problem ( $\# \text{ m}^{-3}$ )
$n_j^C$	number density of particles at the center of size group $j$ ( $\# \text{ m}^{-3}$ )
$n_j^L$	number density of border particles, representing the smallest particles in size group $j$ ( $\# \text{ m}^{-3}$ )
$n_j^R$	number density of border particles, representing the largest particles in size group $j$ ( $\# \text{ m}^{-3}$ )

$r_i, r_j$	characteristic radius of size $i$ particles, or size group $j$ particles (m)	$\varepsilon$	turbulent energy dissipation rate ( $\text{m}^2 \text{s}^{-3}$ )
$r_{j-1,j}$	threshold radius to separate size group $j-1$ and size group $j$ particles in PSG method (m)	$\mu_M, \mu_P, \mu_I$	shear modulus of the matrix, precipitate phase, and interface (Pa)
$r_c$	the critical radius for nucleation (m)	$\nu_M, \nu_P$	Poisson's ratio of the matrix and precipitate phases
$\bar{r}_P$	average precipitate particle size (m)	$\rho_{\text{steel}}, \rho_P$	density of steel matrix and precipitate phase ( $\text{kg m}^{-3}$ )
$t$	time (s)	$\sigma$	interfacial energy between precipitated particle/matrix ( $\text{J m}^{-2}$ )
$\Delta t$	time step size in numerical computation (s)	$\sigma_c$	chemical interfacial energy between precipitated particle/matrix ( $\text{J m}^{-2}$ )
$w_P^e$	equilibrium mass concentration of precipitate phase (wt pct)	$\sigma_{\text{st}}$	structural interfacial energy between precipitated particle/matrix ( $\text{J m}^{-2}$ )
$A_i, A_j$	the surface area of size $i$ particles, or size group $j$ particles ( $\text{m}^2$ )	$\nu$	kinematic viscosity ( $\text{m}^2 \text{s}^{-1}$ )
$A_M$	atomic mass unit of element M ( $\text{g mol}^{-1}$ )	$\varphi_P$	volume fraction of precipitate phase
$D$	diffusion coefficient of the precipitation in the parent phase ( $\text{m}^2 \text{s}^{-1}$ )	$\Phi_{i,k}$	collision frequency between size $i$ and size $k$ particles ( $\text{m}^3 \#^{-1} \text{s}^{-1}$ )
$D_f$	fractal dimension for precipitate morphology	$\Pi$	supersaturation
$G_M$	number of size groups for the largest agglomerated particle in PSG method	$\Delta E_0$	heat of solution of precipitate in a dilute solution of matrix ( $\text{J mol}^{-1}$ )
$G_T$	truncating size group in PSG method to match experimental resolution	$\Delta G_V$	change of Gibbs free energy per unit volume during precipitation ( $\text{J m}^{-3}$ )
$K$	rate function for nucleation and growth in KJMA model	$\Delta H$	heat of formation of precipitate ( $\text{J mol}^{-1}$ )
$M_0$	total mass concentration of alloying element M in the steel composition (wt pct)		
$[M]$	equilibrium mass concentration of alloying element M (wt pct)		
$N_j$	total number density of size group $j$ particles in PSG method ( $\# \text{m}^{-3}$ )		
$N_A$	Avogadro number ( $6.022 \times 10^{23} \# \text{mol}^{-1}$ )		
$N_M$	total number density of pseudomolecules ( $\# \text{m}^{-3}$ )		
$N_s$	number of atoms per unit area across the interface ( $\# \text{m}^{-2}$ )		
$N_T$	total number density of all particles ( $\# \text{m}^{-3}$ )		
$R_g$	gas constant ( $8.314 \text{ J K}^{-1} \text{ mol}^{-1}$ )		
$R_V$	particle volume ratio between two neighboring particle size groups		
$T$	absolute temperature (K)		
$V_i, V_j$	characteristic volume of size $i$ particles or size group $j$ particles ( $\text{m}^3$ )		
$V_{j-1,j}$	threshold volume to separate size group $j-1$ and size group $j$ particles in PSG method ( $\text{m}^3$ )		
$V_P$	molar volume of precipitated phase ( $\text{m}^3 \text{mol}^{-1}$ )		
$X_M, X_P$	molar concentration of precipitate-forming element in matrix and precipitate phases		
$Z_s$	number of bonds per atom across the interface		
$Z_l$	coordinate number of nearest neighbors within the crystal lattice		
$\alpha_i$	dissociation rate of size $i$ particles ( $\text{m}^2 \text{s}^{-1}$ )		
$\beta_i$	diffusion growth rate of size $i$ particles ( $\text{m}^3 \#^{-1} \text{s}^{-1}$ )		
$\delta$	relative lattice misfit across the interface between pairs of precipitate and matrix atoms		
$\delta_{i,k}$	Kronecker's delta function ( $\delta_{i,k} = 1$ for $i = k$ , $\delta_{i,k} = 0$ for $i \neq k$ )		

## SUPERSCRIPTS

*	dimensionless value
—	average value
L, R, C	left, right border-size, and center-size particles in each size group

## FUNCTIONS

ceil( $x$ )	the smallest integer which is not less than real number $x$
floor( $x$ )	the largest integer which is not larger than real number $x$

## REFERENCES

1. C. Zener: *Trans. Am. Inst. Miner. Metall. Soc.*, 1948, vol. 175, pp. 15–51.
2. M. Hillert: *Acta Metall.*, 1965, vol. 13, pp. 227–38.
3. T. Gladman: *Proc. Roy. Soc. London Ser. A*, 1966, vol. 294, pp. 298–309.
4. P.A. Manohar, M. Ferry, and T. Chandra: *ISIJ Int.*, 1998, vol. 38, pp. 913–24.
5. N. Yoshinaga, K. Ushioda, S. Akamatsu, and O. Akisue: *ISIJ Int.*, 1994, vol. 34, pp. 24–32.
6. E.E. Kashif, K. Asakura, T. Koseki, and K. Shibata: *ISIJ Int.*, 2004, vol. 44, pp. 1568–75.
7. S.C. Park, I.H. Jung, K.S. OH, and H.G. Lee: *ISIJ Int.*, 2004, vol. 44, pp. 1016–23.
8. Y. Li, J.A. Wilson, D.N. Crowther, P.S. Mitchell, A.J. Craven, and T.N. Baker: *ISIJ Int.*, 2004, vol. 44, pp. 1093–1102.
9. R.L. Klueh, K. Shiba, and M.A. Sokolov: *J. Nucl. Mater.*, 2008, vol. 377, pp. 427–37.
10. J.Y. Choi, B.S. Seong, S.C. Baik, and H.C. Lee: *ISIJ Int.*, 2002, vol. 42, pp. 889–93.
11. B.J. Lee: *Metall. Mater. Trans. A*, 2001, vol. 32A, pp. 2423–39.



12. R.C. Hudd, A. Jones, and M.N. Kale: *J. Iron Steel Inst.*, 1971, vol. 209, pp. 121–25.
13. T. Gladman: *The Physical Metallurgy of Microalloyed Steels*, The Institute of Materials, London, UK, 1997, pp. 82–130.
14. W.J. Liu and J.J. Jonas: *Metall. Trans. A*, 1989, vol. 20A, pp. 1361–74.
15. N. Gao and T.N. Baker: *ISIJ Int.*, 1997, vol. 37, pp. 596–604.
16. J.Y. Park, J.K. Park, and W.Y. Choo: *ISIJ Int.*, 2000, vol. 40, pp. 1253–59.
17. K. Xu, B.G. Thomas, and R. O'Malley: *Metall. Mater. Trans. A*, 2011, vol. 42A, pp. 524–39.
18. A.N. Kolmogorov: *Izv. Akad. Nauk SSSR, Ser. Fiz.*, 1937, vol. 1, pp. 335–38.
19. W.A. Johnson and R.F. Mehl: *Trans. AIME*, 1939, vol. 135, pp. 416–42.
20. M. Avrami: *J. Chem. Phys.*, 1939, vol. 7, pp. 1103–12.
21. J.W. Christian: *The Theory of Transformation in Metals and Alloys*, Part I, Pergamon Press, Oxford, UK, 1975.
22. N.Y. Zolotarevsky, V.P. Pletenev, and Y.F. Titovets: *Model. Simul. Mater. Sci. Eng.*, 1998, vol. 6, pp. 383–91.
23. H.C. Kang, S.H. Lee, D.H. Shin, K.J. Lee, S.J. Kim, and K.S. Lee: *Mater. Sci. Forum*, 2004, vol. 449–452, pp. 49–52.
24. M. Smoluchowski: *Z. Phys. Chem.*, 1917, vol. 92, pp. 127–55.
25. P.G. Saffman and J.S. Turner: *J. Fluid Mech.*, 1956, vol. 1, pp. 16–30.
26. U. Lindborg and K. Torssell: *Trans. TMS-AIME*, 1968, vol. 242, pp. 94–102.
27. S.K. Friedlander and C.S. Wang: *J. Colloid Interface Sci.*, 1966, vol. 22, pp. 126–32.
28. V.G. Levich: *Physicochemical Hydrodynamics*, Prentice-Hall, Inc, Englewood Cliffs, NJ, 1962, p. 211.
29. D. Turnbull and J.C. Fisher: *J. Chem. Phys.*, 1949, vol. 17, pp. 71–73.
30. W.J. Liu and J.J. Jonas: *Metall. Trans. A*, 1989, vol. 20A, pp. 689–97.
31. W.J. Liu and J.J. Jonas: *Metall. Trans. A*, 1988, vol. 19A, pp. 1403–13.
32. W. Ostwald: *Lehrbuch der allgemeinen Chemie*, 1896, vol. 2, Leipzig, Germany.
33. I.M. Lifshitz and V.V. Slyozov: *J. Phys. Chem. Solids*, 1961, vol. 19, pp. 35–50.
34. C. Wagner: *Zeitschrift Zeitschr. Elektrochemie*, 1961, vol. 65, pp. 581–91.
35. C. Zener: *J. Appl. Phys.*, 1949, vol. 20, pp. 950–53.
36. K.C. Russell: *Adv. Colloid Interface Sci.*, 1980, vol. 13, pp. 205–318.
37. H.I. Aaronson, L. Laird, and K.R. Kinsman: *Phase Transformations*, Ed. H.I. Aaronson, ASM, Materials Park, OH, 1970, pp. 313–96.
38. M. Kahlweit: *Adv. Colloid Interface Sci.*, 1975, vol. 5, pp. 1–35.
39. J. Miyake and M.E. Fine: *Scripta Metall. Mater.*, 1991, vol. 25, pp. 191–94.
40. R. Kampmann, H. Eckerlebe, and R. Wagner: *Mater. Res. Soc. Symp. Proc.*, 1987, vol. 57, pp. 526–42.
41. L.M. Cheng, E.B. Hawbolt, and T.R. Meadowcroft: *Metall. Mater. Trans. A*, 2000, vol. 31A, pp. 1907–16.
42. F. Perrard, A. Deschamps, and P. Maugis: *Acta Mater.*, 2007, vol. 55, pp. 1255–66.
43. J. Stávek and M. Šípek: *Cryst. Res. Technol.*, 1995, vol. 30, pp. 1033–49.
44. S. Müller, C. Wolverson, L.W. Wang, and A. Zunger: *Europhys. Lett.*, 2001, vol. 55, pp. 33–39.
45. E. Clouet, M. Nastar, and C. Sigli: *Phys. Rev. B*, 2004, vol. 69, p. 064109.
46. C. Hin, B.D. Wirth, and J.B. Neaton: *Phys. Rev. B*, 2009, vol. 80, p. 134118.
47. R. Mukherjee, T.A. Abinandanan, and M.P. Gururajan: *Acta Mater.*, 2009, vol. 57, pp. 3947–54.
48. R. Mukherjee, T.A. Abinandanan, and M.P. Gururajan: *Scripta Mater.*, 2010, vol. 62, pp. 85–88.
49. Y. Tsukada, A. Shiraki, Y. Murata, S. Takaya, T. Koyama, and M. Morinaga: *J. Nucl. Mater.*, 2010, vol. 401, pp. 154–58.
50. J. Svoboda, F.D. Fischer, P. Fratzl, and E. Kozeschnik: *Mater. Sci. Eng. A*, 2004, vol. 385, pp. 166–74.
51. E. Hozeschnik, J. Svoboda, P. Fratzl, and F.D. Fischer: *Mater. Sci. Eng. A*, 2004, vol. 385, pp. 157–65.
52. E. Kozeschnik, J. Svoboda, R. Radis, and F.D. Fischer: *Model. Simul. Mater. Sci. Eng.*, 2010, vol. 18, p. 015011.
53. E. Clouet, A. Barby, L. Laé, and G. Martin: *Acta Mater.*, 2005, vol. 52, pp. 2313–25.
54. J. Lepinoux: *Acta Mater.*, 2009, vol. 57, pp. 1086–94.
55. J. Lepinoux: *Philos. Mag.*, 2010, vol. 90, pp. 3261–80.
56. L. Kampmann and M. Kahlweit: *Ber. Bunsenges. Phys. Chem.*, 1970, vol. 74, pp. 456–62.
57. J. Zhang and H. Lee: *ISIJ Int.*, 2004, vol. 44, pp. 1629–38.
58. Y.J. Kwon, J. Zhang, and H.G. Lee: *ISIJ Int.*, 2008, vol. 48, pp. 891–900.
59. N. Zhang and Z.C. Zheng: *J. Phys. D: Appl. Phys.*, 2007, vol. 40, pp. 2603–12.
60. Y. Miki, B.G. Thomas, A. Denisov, and Y. Shimada: *Ironmaker Steelmaker*, 1997, vol. 24, pp. 31–38.
61. Y. Miki and B.G. Thomas: *Metall. Mater. Trans. B*, 1999, vol. 30B, pp. 639–54.
62. L. Zhang, S. Taniguchi, and K. Cai: *Metall. Mater. Trans. B*, 2000, vol. 31B, pp. 253–66.
63. D. Sheng, M. Söder, P. Jönsson, and L. Jonsson: *Scand. J. Metall.*, 2002, vol. 31, pp. 134–47.
64. M. Hallberg, P.G. Jönsson, T.L.I. Jonsson, and R. Eriksson: *Scand. J. Metall.*, 2005, vol. 34, pp. 41–56.
65. T. Nakaoka, S. Taniguchi, K. Matsumoto, and S.T. Johansen: *ISIJ Int.*, 2001, vol. 41, pp. 1103–11.
66. L. Zhang and W. Pluschkell: *Ironmaking Steelmaking*, 2003, vol. 30, pp. 106–10.
67. F. Gelbard, Y. Tambour, and J.H. Seinfeld: *J. Colloid Interface Sci.*, 1980, vol. 76, pp. 541–56.
68. J.J. Wu and R.C. Flagan: *J. Colloid Interface Sci.*, 1988, vol. 123, pp. 339–52.
69. H. Tozawa, Y. Kato, K. Sorimachi, and T. Nakanishi: *ISIJ Int.*, 1999, vol. 39, pp. 426–34.
70. K. Higashitani, Y. Yamauchi, Y. Matsuno, and G. Hosokawa: *J. Chem. Eng. Jpn.*, 1983, vol. 116, pp. 299–304.
71. F. Vodopivec: *J. Iron Steel Inst.*, 1973, vol. 211, pp. 664–65.
72. H.F. Beeghly: *Ind. Eng. Chem.*, 1942, vol. 14, pp. 137–40.
73. T. Gladman: *The Physical Metallurgy of Microalloyed Steels*, The Institute of Materials, London, UK, 1997, pp. 206–07.
74. H. Oikawa: *Tetsu-to-Hagane*, 1982, vol. 68, pp. 1489–97.
75. W.C. Leslie, R.L. Rickett, C.L. Dotson, and C.S. Walton: *Trans. Am. Soc. Metall.*, 1954, vol. 46, pp. 1470–99.
76. F.G. Wilson and T. Gladman: *Int. Mater. Rev.*, 1988, vol. 33, pp. 221–86.
77. R. Radis and E. Kozeschnik: *Mater. Sci. Forum*, 2010, vols. 636–637, pp. 605–11.
78. R. Radis and E. Kozeschnik: *Model. Simul. Mater. Sci. Eng.*, 2010, vol. 18, p. 055003.
79. F. Perrard, A. Deschamps, F. Bley, P. Donnadiou, and P. Maugis: *J. Appl. Crystallogr.*, 2006, vol. 39, pp. 473–82.
80. J. Geise and C. Herzig: *Z. Metallkd.*, 1985, vol. 76, pp. 622–26.
81. T. Gladman: *The Physical Metallurgy of Microalloyed Steels*, The Institute of Materials, London, UK, 1997, pp. 82–130.
82. E.K. Storrs and N.H. Krikorian: *J. Phys. Chem.*, 1960, vol. 64, pp. 1471–77.
83. S.M. He, N.H. Van Dijk, M. Paladugu, H. Schut, J. Kohlbrecher, F.D. Tichelaar, and S. Van Der Zwaag: *Phys. Rev. B*, 2010, vol. 82, p. 174111.
84. F.F. Abraham: *Homogeneous Nucleation Theory*. Academic Press, New York, NY, 1974.
85. B. Dutta and C.M. Sellars: *Mater. Sci. Technol.*, 1987, vol. 3, pp. 197–206.
86. J.P. Michel and J.J. Jonas: *Acta Metall.*, 1981, vol. 29, pp. 513–26.
87. A. LE Bon, J. Rofes-Vernis, and C. Rossard: *Met. Sci.*, 1975, vol. 9, pp. 36–40.
88. A.R. Jones, P.R. Howell, and B. Ralph: *J. Mater. Sci.*, 1976, vol. 11, pp. 1600–06.
89. D. Turnbull: *Impurities and Imperfections*, Seminar Proceedings, ASM, Cleveland, OH, 1955, pp. 121–44.
90. W.J. Liu and J.J. Jonas: *Mater. Sci. Technol.*, 1989, vol. 5, pp. 8–12.
91. J.H. Van Der Merwe: *J. Appl. Phys.*, 1963, vol. 34, pp. 117–22.
92. R.G. Baker and J. Nutting: *Precipitation Process in Steels, Special Report No. 64*, The Iron and Steel Institute, London, UK, 1959, pp. 1–22.
93. H. Shoji: *Z. Kristallogr.*, 1931, vol. 77, pp. 381–410.

94. Z. Nishiyama: *Science Report, Tohoku Imperial Univ.*, 1936, vol. 25, p. 79.
95. W.G. Burgers: *Physica*, 1934, vol. 1, pp. 561–86.
96. N.W. Chase, Jr.: *NIST-JANAF Thermochemical Tables*, 4th ed., *J. Phys. Chem. Ref. Data*, 1998, pp. 1–1951.
97. L.E. Toth: *Transaction Metal Carbides and Nitrides*, Academic Press, New York, NY, 1971.
98. H.J. Frost and M.F. Ashby: *Deformation-Mechanism Maps*, Pergamon Press, Oxford, UK, 1982, pp. 20–70.
99. L.M. Cheng, E.B. Hawbolt, and T.R. Meadowcroft: *Metall. Mater. Trans. A*, 2000, vol. 31A, pp. 1907–16.
100. L.R. Zhao, K. Chen, Q. Yang, J.R. Rodgers, and S.H. Chiou: *Surf. Coat. Technol.*, 2005, vol. 200, pp. 1595–99.